High-Resolution Near-Field Optical Microscopy of Biological Molecules on Gold Surfaces

Dissertation
der Mathematisch-Naturwissenschaftlichen Fakultät
der Eberhard Karls Universität Tübingen
zur Erlangung des Grades eines
Doktors der Naturwissenschaften
(Dr. rer. nat.)

vorgelegt von
Dipl.-Phys. Laura E. Hennemann
aus Stuttgart

Tübingen
2011

Tag der mündlichen Qualifikation: 18. Juli 2011
Dekan: Prof. Dr. Wolfgang Rosenstiel
Erstgutachter: Prof. Dr. Alfred J. Meixner
Zweitgutachter: PD Dr. Marc Brecht

'Physicists suffer the genetic defect of optimism.' Leon M. Lederman

Contents

List of Abbreviations

AFM	atomic force microscopy
APD	avalanche photo-diode
a.u.	arbitrary units
CCD	charge-coupled device
DDA	discrete dipole approximation
DIP	diindenoperylene
DNA	deoxyribonucleic acid
FDTD	finite difference time-domain
FWHM	full width at half maximum
HeNe	helium-neon laser
HEWL	hen egg white lysozyme
HOMO	highest occupied molecular orbital
LSP	localised surface plasmon
LUMO	lowest unoccupied molecular orbital
NA	numerical aperture
OD	optical density
PL	photoluminescence
SEM	scanning electron microscopy
SERS	surface-enhanced Raman scattering
SERRS	surface-enhanced resonance Raman scattering
SNOM	scanning near-field optical microscopy
SPM	scanning probe microscopy
STED	stimulated emission depletion
STM	scanning tunnelling microscopy
TERS	tip-enhanced Raman scattering
UV	ultraviolet

1 Introduction

A fundamental part of nano-technology is imaging the nano-world — be it man-made nano-structures or natural specimens such as organic molecules. Scanning probe microscopical methods like atomic force microscopy (AFM) [Bin86] or scanning tunnelling microscopy (STM) [Bin82] accomplish a lot in characterising surfaces. Since their invention almost thirty years ago, the possibilities of these methods continue to fascinate scientists and laymen alike. They have already extended to the investigation of biological molecules. With a shear-force AFM setup, astounding images of the organic structure of a single molecule were recently obtained [Gro10]. Even the partial sequencing of an individual DNA strand using STM has been demonstrated [Tan09]. However, conventional AFM and STM methods lack the ability to investigate the direct interaction of a sample with light.

And why would we be interested in measuring with light? One answer is that living organisms and biological molecules have evolved to respond explicitly to the visible light range of the sun. Colour recognition by the human eye is an apparent example of this [Gar10]. In the lab, Raman spectroscopy [Ram28] is one method to collect optical information of specimen molecules.

Conventional optical microscopes on the other hand fail to image the nano-scale. The reason for this is that optical resolution is diffraction limited. This means that simply increasing the magnification of a conventional microscope more and more will not work. Roughly speaking, an optical microscope cannot recognise two points on a surface as two separate ones if they are closer together than half the wavelength of the employed light. With visible light wavelengths ranging approximately from 400 nm to 800 nm, one solution would be to use light of a shorter wavelength – which is the idea that triggered amongst others the development of the Blu-ray Disc. By using the UV range and even smaller wavelengths, or by employing the wave nature of a high-energy beam of electrons in a scanning electron microscope (SEM), the diffraction limit can be pushed to smaller scales. Yet as just noted, it is exactly the visible light region which we are often interested in.

Hence, the ideal setup would be one that combines the advantages of AFM resolution and optical information. This is indeed accomplished in scanning near-field optical microscopy (SNOM) [Dom10]. Such microscopes feature a fine tip functioning both as an AFM-like topographical probe and as an optical antenna. In its latter function,

the tip couples the light energy into the nano-scale area between the tip apex and the sample.

To date, however, only few SNOM instruments are commercially available and even these are not simple plug-and-play devices for routine measurements. The vast majority of state-of-the-art scientific results is still produced with custom-built SNOM setups.

A Short History of Scanning Near-Field Optical Microscopy

As early as 1928, Irish scientist Edward Synge proposed a method to overcome the classical optical resolution limit. He exchanged several letters with Albert Einstein – see figure 1.1 – in which he described two ideas. The first was to put a small metal particle in the focus of a lens and collect the particle's stray light. The second suggestion involved a very fine hole in an otherwise opaque device. This aperture should be smaller that the wavelength of the light and it should be raster-scanned over a sample surface [Syn28]. Synge even foresaw the use of piezo-electric devices for fast scanning with high lateral precision [Syn32].

Yet in terms of a technical realisation, Synge was ahead of his time. Only in the mid-1980s, his second idea began to be fulfilled in the form of aperture SNOM. The work of Dieter Pohl et al. probably counts as the first aperture-SNOM experiment [Poh84]. They covered a quartz crystal tip with metal layers and created a nano-scale aperture at the tip apex. Today, the optical resolution of this technique has reached approximately 45 nm [Neu11].

A drawback of aperture SNOM however is an intrinsic problem: to obtain a higher resolution, the aperture should be made as small as possible. Yet the smaller it is, the less light can pass. The excitation and the collected signal thus get weaker.

In 1985, John Wessel re-invented and advanced the first of Synge's ideas as a complementary principle to aperture SNOM [Wes85]. He evaluated the concept of scanning

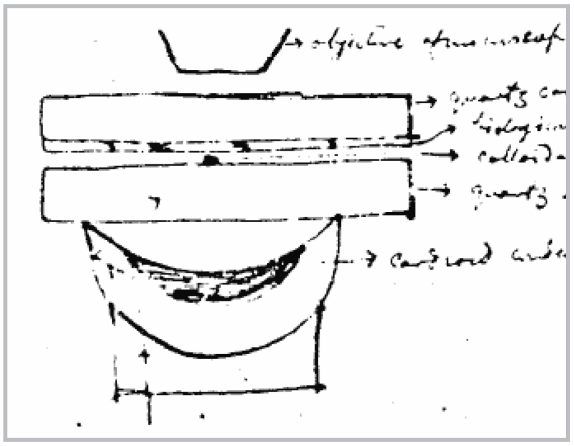

Figure 1.1: A drawing by Edward Synge in his first letter to Albert Einstein in April 1928. His sketch shows a metal nano-particle on a glass slide put into the focus of a Zeiss cardioid condenser. The metal particle would thus act as a probe for a biological sample which was to be attached onto a second glass slide above the nano-particle. Taken from [Gol07].

a metallic nano-particle over a sample surface. Simultaneously, the particle should be illuminated by a laser. Wessel knew that the laser could excite so-called particle plasmons – quantised oscillations of the free electrons of the metal – in the nano-particle. Plasmon resonances lead to strong electric fields at the particle surface. As envisioned by Wessel, the metal nano-particle would thus act as an optical antenna. He proposed to use this plasmonic antenna to collect among others locally enhanced optical Raman signals of the sample. This technique would later be known as tip-enhanced Raman scattering (TERS).

The actual assembly was realised years later employing a fine metal tip instead of a nano-particle, whilst the tip apex assumes the same role of generating a localised electric field. First successful experiments were reported in the 1990s [Zen95], soon combining SNOM and TERS [Stö00].

Moving on from history [Nov07, Dom10] to state-of-the-art experiments [Har08, Dec09], many different samples have been studied by SNOM and TERS over the past decade. These include amongst others single-walled carbon nano-tubes [Har03], poly-cytosine RNA strands [Bai08], single brilliant cresyl blue molecules [Ste08], graphene layers [Sai09], edges of molecular films [Zha10] and domains of organic solar cell films [Wan10]. This incomplete list illustrates that this technique is of interest for various research fields.

Inelastic light scattering as discovered by the Indian physicist Chandrasekhar Raman and the principle of SNOM invented by the Irishman Edward Synge here come to a unique combination. It allows us to study interactions of molecules with light at nanometre-resolution. Incidentally, Raman and Synge made their discoveries in the same year 1928. What they initiated keeps scientists busy until now. Undoubtedly, many more SNOM and TERS investigations will follow in the years to come.

1.1 Motivation of this Work

One of the few custom-made apertureless SNOM setups was built in the research group of Professor Meixner where I conducted the work presented here. With this setup [Zha09], we aim to investigate individual molecules under conditions as close to their natural conformation as possible. This includes the ambient working conditions in air and at room temperature. It also comprises not attaching fluorescent markers to the molecules. Furthermore, due to the top-illumination by a parabolic mirror, we are able to use a vast number of substrates including non-transparent ones. We can thus work with substrates the molecules easily bind to by themselves.

The main information we gather from the molecules is their individual Raman spectrum. The Raman bands are associated so closely to each kind of molecule that they

can be called a Raman fingerprint. In order to enhance the intrinsically weak Raman signal, we can perform surface-enhanced Raman scattering (SERS) by choosing appropriate substrates. Alternatively – and this is a key tool in apertureless scanning near-field optical microscopy – we can collect tip-enhanced Raman signals with our SNOM tip.

The aim of this work was to establish the investigation of biological molecules on our SNOM setup. The objective was to measure such molecules both by SERS in confocal mode and by TERS in the SNOM mode of our setup.

Via plasmon resonances, the electric field can be enhanced by metal nano-particles as well as by sharp edges [Sun05]. As SERS substrates, I hence employed evaporated rough metal edges which had previously proven to be effective enhancers [Sac08a] and additional nano-particles. For a more systematic approach, I also examined regular arrays of gold nano-triangles – so-called Fischer patterns. I first studied the plasmonic behaviour of such triangle arrays extensively in order to later employ them as SERS substrates.

Of the large variety of biological molecules, deoxyribonucleic acid (DNA) is probably the best-known molecule [Wat53]. Hence, one of the main motivations of this work was the investigation of DNA by SNOM. The diameter of a DNA double strand is a few nanometres and thus large enough that it can be imaged topographically by our setup. Employing TERS, the aim was to then collect Raman spectra of individual DNA double strands.

Up to now, the investigation of DNA such as genome sequencing or determination of DNA-drug interactions is done in measurements with many molecules. In such ensemble measurements, individual effects are inaccessible. In ensemble Raman investigations for example, locally and temporally restricted molecular processes will not be observable, since their Raman lines are smeared out. Additionally, weaker signals can easily be covered by stronger ones.

The study of individual DNA molecules would thus yield new and revealing insights. As was recently suggested, the sequencing of single DNA strands might even become possible with SNOM and TERS [Bai08]. The interaction of a DNA strand with drug molecules or with a single protein could also become observable with these methods.

A third project conducted during the course of this work were experiments on slightly larger clusters of biological molecules: protein amyloid fibrils [Dob03]. These, too, were to be investigated by SNOM and TERS.

Many, if not all proteins can form such amyloid fibrils. These fibrils are approximately 10 nanometres thick and believed to be responsible for a variety of medical conditions such as Alzheimer's disease. However, there are also several types of functional amyloid that are produced e.g. by yeast [Ham08]. In some cases, the

producing organism effectively protects itself from the folding intermediate of the amyloid. A deeper understanding of amyloid formation and amyloid fibrils might thus lead us to better comprehend the respective diseases and even one day give us hints for therapeutic strategies.

1.2 Outline of this Thesis

In the upcoming chapter 2, I will explain the theoretical fundamentals of optical resolution both in the far-field and in the near-field case. To understand the latter, some theory about plasmonic excitation will be given. Furthermore, I will resolve the general mechanism of Raman scattering as well as its signal enhancement in surface-enhanced Raman scattering (SERS) and in tip-enhanced Raman scattering (TERS). Additionally, an overview on the state of research in the topics investigated in this thesis will be given.

In chapter 3, I will then introduce the scanning near-field optical microscopy (SNOM) setup on which all of the experiments presented later were conducted. This will include some more theory on optics to explain the use of certain components. The chapter will conclude with an illustration of a typical experimental routine as performed on our setup.

In the following three chapters 4, 5 and 6, I will elaborate on the experiments done during the course of this work. In each of these chapters, I will explain the particular sample preparation, state the results obtained in different measurements and discuss these results. Chapter 4 will be about the plasmonics of nano-triangles arranged in so-called Fischer patterns and how to use them as SERS substrates. Chapter 5 describes my diverse measurements on individual DNA double strands. Chapter 6 then deals with slightly larger biological structures: amyloid fibrils of proteins.

I will give final conclusions in chapter 7. Here, I will also outline future possibilities to expand and deepen the insight found in the course of this work.

2 Theoretical Fundamentals and State of Research

Resolution is arguably the most important parameter in microscopy. It is the ability to distinguish two nearby points on a sample as two separate ones. In optical microscopy, the resolution limit was long linked to the wavelength of the employed light by the diffraction limit. Advances like stimulated emission depletion (STED) microscopy [Hel94] and not least near-field optics have constantly shrunk the resolution limit and finally decoupled it from wavelength restraints.

This section illustrates the theory of the classical optical resolution limit and how to overcome it. It explains the Raman spectroscopic methods which I used in my investigations and introduces the field of plasmonics. Finally, I will also give a summary of the current state of research in the specific fields of this work.

2.1 Optical Resolution I: Conventional Microscopy

In classical optical microscopy, the resolution is limited by diffraction. Light can never be focused to a single point in the image plane but only to an area described by the point-spread function of the optical system. Geometrically, this is depicted by the Airy disc, see figure 2.1. The distance from the point-spread function's absolute maximum to its first minimum is denoted by Δx. This is also the radius of the Airy disc and is given by

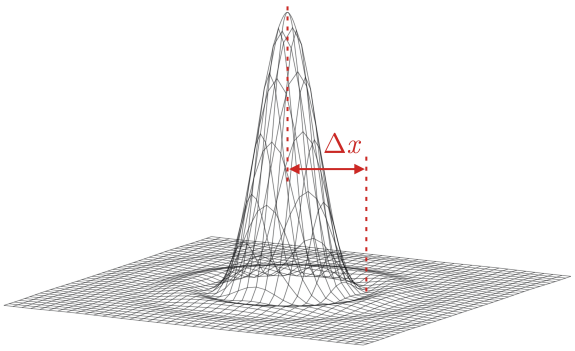

Figure 2.1: Plot of an Airy disc. The bottom plane is the image plane, whilst the height depicts the intensity.

$$\Delta x = 0.61 \frac{\lambda}{\mathrm{NA}} \qquad \text{with} \qquad \mathrm{NA} = n \cdot sin(\theta_{max}) \; . \tag{2.1}$$

Here, NA stands for the numerical aperture of the focusing lens and θ_{max} is the maximal angle between focusing beam parts and the optical axis.

In 1896, Lord Rayleigh suggested a criterion for the resolution limit in optical microscopy, stating that two points can only be resolved if the central maximum of the Airy disc of the first point is located at least in the first minimum of the Airy disc of the second point [Ray96]. This corresponds exactly to the radius Δx of the Airy disc and hence Δx is also the resolution limit according to the Rayleigh criterion. Ernst Abbe had given a similar reasoning already some decades earlier [Abb73].

2.2 Plasmonics

The relatively new research field called plasmonics investigates the interaction of light with metallic surfaces. More precisely, the coupling of photons with plasmons in the material. A plasmon is a quantised oscillation of the charge-density. It occurs in a plasma, i.e. in an electrically neutral state in which some of the charges can move freely, such as it is the case in the conduction band of a metal.

However, under normal circumstances, such a coupling of photons with plasmons is not possible, since there is no energy ($E \propto \omega$) and momentum (k) match between the dispersion relation of the two; see figure 2.2. While this finding remains true for plasmons in the bulk material, surface plasmons can be excited under certain conditions. This can be done e.g. using the Kretschmann configuration and exciting a metal film through an underlying glass prism [Kre71]. This means using light with a less steep dispersion relation $\omega' = ck/n$, where n would be the refractive index of the glass, and thus obtaining an intersection point of ω and k.

The second approach to excite surface plasmons is to introduce a periodic structure on the sample surface [Jel87]. Regarding the periodicity as a grating with a grating constant a, it has a reciprocal lattice component $g = 2\pi/a$. This can be added – even multiple times – to a component of the wave vector $\vec{k}$ of the light dispersion line in order to reach the larger impulse k_{SP} of the surface plasmon [Rae88]:

$$k_{SP} = \frac{\omega}{c} + N \cdot \frac{2\pi}{a} \tag{2.2}$$

with N being any integer.

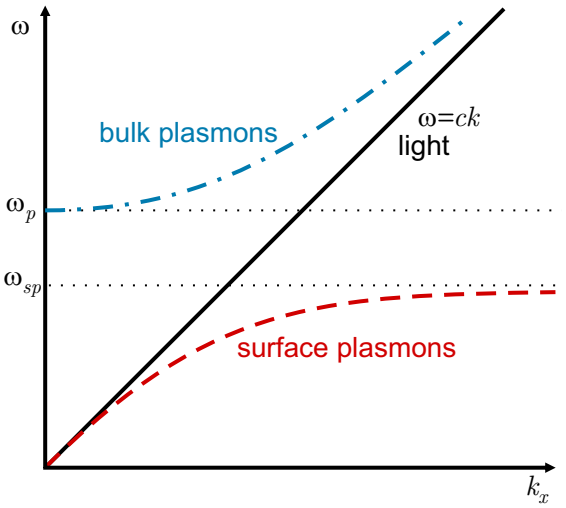

Figure 2.2: Dispersion relation of light in free space, of bulk plasmons and of surface plasmons. ω denotes the angular frequency of the waves and k_x the wave vector component. ω_p is the plasma frequency, whilst $\omega_{sp} = \omega_p/\sqrt{2}$ is the limit of the surface plasmon frequency.

A randomly rough surface will lead to the same effect since it can be regarded as a superposition of many periodicities. Surface plasmons excited in this way play a significant role in surface-enhanced Raman scattering (SERS, see chapter 2.4.1).

In analogy to plasmonic modes in surface roughnesses, plasmons can also be excited in nano-particles. Such *particle plasmons* are sometimes also called localised surface plasmons (LSP). The visible optical properties of metallic nano-particles are dominated by such plasmonic excitations: depending on size and shape, the absorption maximum is located at different wavelengths. Thus, the particles can exhibit plasmonic resonances throughout the whole spectral range.

For a theoretical description [Kre95, Web07], we start by considering the polarisation $\vec{P}$ of a sphere. It is linked to the exciting electric field $\vec{E}_0$ by the polarisability α:

$$\vec{P} = \alpha \vec{E}_0 \qquad \text{with} \qquad \alpha = 4\pi\epsilon_0 R^3 \frac{\epsilon - \epsilon_m}{\epsilon + 2\epsilon_m}\,, \tag{2.3}$$

where ϵ is the static dielectric constant of the sphere and ϵ_m that of the surrounding medium.

This classical electrodynamic approach may be applied to metallic spheres of radius R in an oscillating electromagnetic field of wavelength λ under the following conditions and assumptions:

- $R \ll \lambda$: At any given time, the phase of the external electromagnetic wave is constant over the extension of the particle. This is called the quasi-static regime, see figure 2.3.

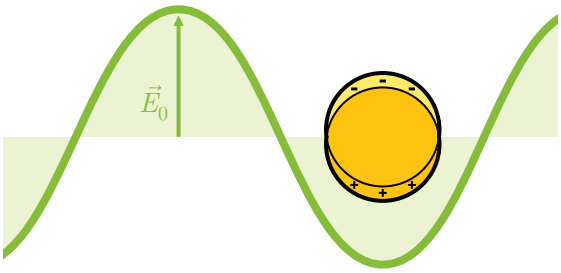

Figure 2.3: Sketch of an electromagnetic wave exciting a dipolar plasmon inside a metallic nano sphere.

- The magnetic field of the wave has no effect on the particle, i.e. the permeability $\mu = 1$. This is a reasonable assumption for the visible spectral range.
- The complex dielectric function $\epsilon = \epsilon(\omega) = \epsilon_1(\omega) + i\epsilon_2(\omega)$ describes the material of the particle, whereas the medium surrounding the particle has a constant dielectric function ϵ_m.

The polarisation inside the particle can be excited resonantly when $\epsilon + 2\epsilon_m$, the denominator of α in equation 2.3, takes a minimum value. With a complex dielectric function for the particle, this yields

$$(\epsilon_1(\omega) + 2\epsilon_m)^2 + (\epsilon_2(\omega))^2 = min\ . \tag{2.4}$$

Furthermore assuming that close to the resonance the damping is small and hence $\epsilon_2(\omega)$ is small, the resonance condition can be rewritten as

$$\epsilon_1(\omega) = -2\epsilon_m\ . \tag{2.5}$$

However, for larger particles to which $R \ll \lambda$ does not apply, the inner field distribution has to be considered as non-homogeneous. Gustav Mie proposed a general solution to this in 1908 [Mie08]. Using appropriate boundary conditions, he applied the Maxwell equations in spherical coordinates and performed multipole expansions. Additionally to the dielectric functions of the sphere and the surrounding medium, the particle radius R is a further parameter in the Mie theory.

The Mie theory derives a set of equations describing the absorption cross section σ_{abs}, the scattering cross section σ_{sca} and the extinction cross section σ_{ext} of a particle. The notation of cross sections simply compares the intensity loss of a homogeneous and parallel light beam by a single nano-particle to the loss by an ideally absorbing surface of an area σ. It can vary greatly from the actual surface of the nano-particle. The total intensity loss σ_{ext} is the sum of dissipative losses σ_{abs} and elastically scattered σ_{sca} light: $\sigma_{ext} = \sigma_{abs} + \sigma_{sca}$.

Assuming a homogeneous density of nano-particles $n = N/V$ (with N being the absolute number and V the volume), the intensity loss ΔI depends on the distance z the light travels through and is given by the Lambert-Beer law

$$\Delta I(z) = I_0 \cdot \left(1 - e^{-nz\sigma_{ext}}\right) . \tag{2.6}$$

Through a lengthy formalism, the Mie theory can give an exact solution for σ_{ext}. Beyond simple geometries, results of this problem are nowadays mostly computed.

For gold nano-spheres, they show a single dipolar extinction maximum for small particles – just as we found it in equation 2.5. As the particles' sizes grow, this maximum broadens and shifts to the red. Then, a second peak appears at the blue-shifted side of the dipolar peak. This additional maximum is associated to the quadrupole mode that now becomes excitable in the spherical particle.

The greater the particles' shapes deviate from a sphere, the more complex they become to consider. For rod-shaped particles this is still feasible: two peaks associated to the two main axes occur. If the resonance of the long axis is hit, the particle can act as an optical antenna [Müh05, Dor10]. For triangular shapes, simulations have to be performed in order to plot the field distribution [Kol11].

2.3 Optical Resolution II: Near-Field Microscopy

Two expressions are often used when describing the theory of scanning near-field optical microscopy (SNOM[1]): *evanescent fields* and the *near field*. The latter is a simple definition: around the surface of a dipole emitting a wavelength λ, the region with the extent $r \ll \lambda$ is called the near field region. Here, the emitted light has not yet developed as a classical wave but is present only as field strength: the evanescent[2] field. Characteristically for the evanescent field is its exponentially decaying field strength when moving away from the surface of the emitter. An evanescent field can be described by a plane wave

$$\vec{E} = \vec{E_0}\, e^{i(\vec{k}\vec{r} - \omega t)} \tag{2.7}$$

where at least one vector component of $\vec{k}$ is imaginary [Nov06]. This component defines the direction of evanescence in which the wave does not propagate but instead decays.

[1] NSOM, standing for 'near-field scanning optical microscopy', is a synonym of SNOM.

[2] *Evanescere* is a Latin verb meaning 'to fade.'

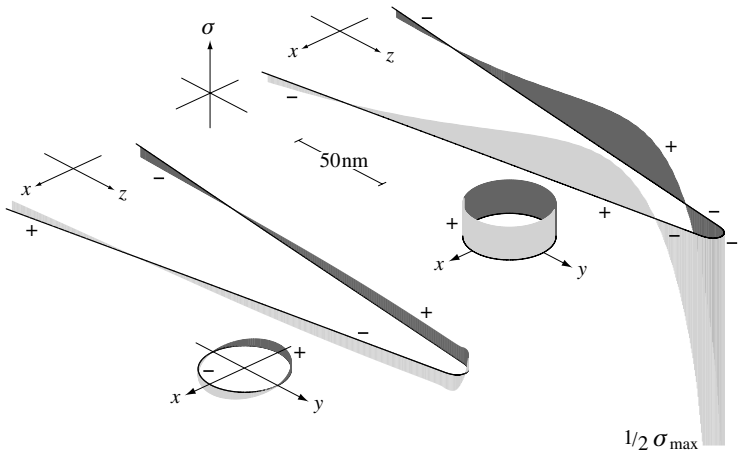

Figure 2.4: Plasmonic modes excitable in a metal tip. Left, the surface charge density σ induced by light with $\vec{E}$ in direction of x; right, with $\vec{E}$ in y. In the second case, surface charges accumulate at the tip apex, leading to a strong near field in the immediate vicinity. Taken from [Nov97, Nov98].

Edward Synge was the first to propose an evanescent-field method to overcome the optical diffraction limit [Syn28]. He suggested a setup where the sample was illuminated through a minute hole in an otherwise opaque plate. This hole should be smaller than the wavelength and its dimensions would then define the resolution of the measurement. Synge's idea failed to become more than a theory within his time. Yet the same principle is nowadays used in aperture SNOM [Poh84, Neu11]. Here, a fine glass fibre tip with a nano-scale aperture is employed. However, to achieve a reasonable illumination intensity, the aperture size cannot be decreased below approximately 45 nm. This dimension hence is a lower limit to the resolution of aperture SNOM. So-called apertureless SNOM[3] on the other hand employs a metal tip as an optical antenna and can thus reach higher resolutions.

Evanescent fields can be generated by total internal reflection [Mei94] or by plasmonic excitation as just discussed in chapter 2.2. Working with the near field of plasmonic objects, we can make use of the energy of the light without being hindered by the diffraction limit.

Strong, localised near fields are also called 'hot spots'. In fact, when conveniently illuminating a sharp metal tip to generate a near field, the evanescent 'hot spot' field at the tip apex is so much stronger than the primary focal field that is used to excite the tip, that the latter may become a negligible background. This holds especially true for the investigation of low concentrated molecules on flat metallic surfaces. Then, since the size of the tip apex defines the size of the evanescent field, it also defines the resolution of the thus performed scanning near-field optical microscopy.

For a thorough theoretical description of how the necessary near field at the tip apex can be generated by different Hermite-Gaussian laser modes see [Nov98]. As can be

[3] In this work, SNOM alone shall always stand for the apertureless SNOM variant.

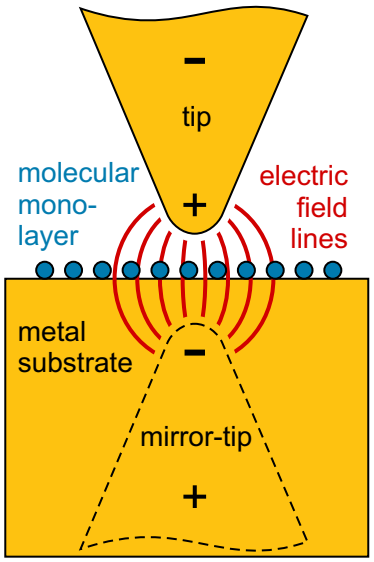

Figure 2.5: Plasmonic gap mode: when approaching a plasmonically excited metal tip to a metal surface, the neutral charge distribution inside the metallic substrate will rearrange due to electrostatic forces. The tip and its mirror image then couple, creating an especially strong near field between them. The + and − signs symbolize the dipole arising inside the tip.

seen in figure 2.4, it is crucial to match the direction of $\vec{E}$ to the axis of the employed tip. This way, the tip is turned into an antenna in the optical electromagnetic range.

'Hot spots' with especially high field strengths occur in gaps between two coupling plasmonic objects [Jun09, Kim09]. Sundaramurthy et al. studied the gap mode enhancement between two gold triangles (a so-called bow-tie configuration) both theoretically and experimentally [Sun05]. However, a single plasmonic tip approached closely to a metal surface will yield a very similar result, since the charge oscillations inside the tip will induce mirror charges in the extended metal below, see figure 2.5 [Sac08b, Pet09]. Yet due to the exponential decay of the near field, a very narrow and moreover highly stable gap distance is required in experiments.

To this end, the feedback design of atomic force microscopy (AFM) [Bai08], scanning tunnelling microscopy (STM) [Pet04, Sta10] or shear-force microscopy [Har03, Zha09] have all been employed successfully. Just like the topographical resolution, the optical resolution obtained is mainly determined by the size of the tip apex [Nov97]. Thus, optical resolutions of $10 - 20\,\mathrm{nm}$ are achieved, a range far below the diffraction limit (recall chapter 2.1).

2.4 Raman Scattering

The scattering of light is its redirection when hitting a piece of matter. Let's consider a piece of matter consisting of molecules. As the molecules interact with the light waves, their electron orbitals are perturbed periodically with the frequency ω_0 of the incident light. This oscillating charge separation is an induced dipole moment. As

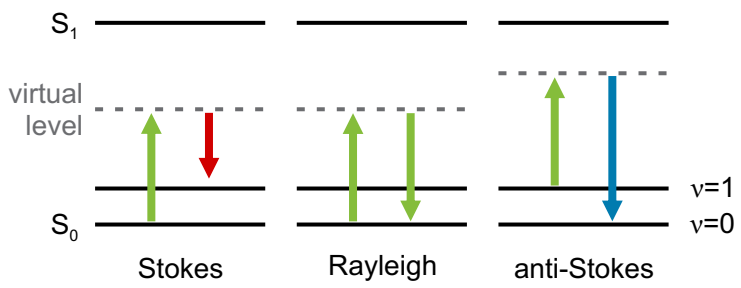

Figure 2.6: Energy diagram for the three cases of Raman scattering of a molecule: Stokes, Rayleigh and anti-Stokes. The colour is symbolic for the frequency-shift towards red or blue.

any oscillating dipole, it is itself again a source of electromagnetic radiation, thus emitting scattered light. Most of it will be emitted elastically at the same frequency ω_0 in a process called *Rayleigh scattering*.

However, a small fraction of the light is scattered inelastically by *Raman scattering*, named after Chandrasekhara Raman who first described it in 1928 [Ram28]. In Raman scattering, the emitted light will be either at $\omega_S < \omega_0$ or at $\omega_{AS} > \omega_0$, with S standing for Stokes and AS for anti-Stokes scattering. *Stokes scattering* is observed when the molecule is in a vibrationally higher excited state after the scattering. In this sense, Stokes scattering is similar to infrared scattering. However, due to selection rules, infrared spectroscopy and Raman spectroscopy yield complementary results. The second case, called *anti-Stokes scattering*, can only occur if the molecule was in an excited state before and is in an energetically lower state after the re-emission. Sketched as an energy diagram, see figure 2.6, the absorption of the incoming photon excites the molecule to a virtual energy level. If by chance the photon energy fits exactly for the molecule to reach an actual energy level, the much stronger *resonance Raman scattering* takes place. In any case, a Raman spectral line corresponding to one specific molecular excitation will always have the same frequency-shift with respect to the incident frequency[4].

Since the vibrations excitable within a given molecule are highly characteristic, Raman scattering yields unique spectroscopic fingerprints of the molecules under investigation. Its downside, however, is its intrinsically low intensity, or put otherwise, the low Raman scattering cross section of only $\sigma \approx 10^{-30} - 10^{-25}\,\mathrm{cm}^2/\mathrm{molecule}$, with the larger values only achieved in resonance Raman scattering [Kne99]. Surface-enhanced Raman scattering (SERS) or tip-enhanced Raman scattering (TERS) are two possible solutions to achieve considerably stronger signals.

[4]This constant frequency-shift justifies the representation of Raman band positions in units of relative inverse centimetres. $0\,\mathrm{cm}^{-1}$ then corresponds to the particular excitation laser wavelength, but the Raman lines given can be reproduced with any other laser. In this thesis, cm^{-1} should always be read as '*relative* inverse centimetres'.

2.4.1 Surface-Enhanced Raman Scattering

The enhancing effect of rough metal structures on the Raman signal was first observed by Fleischmann et al. in 1974 [Fle74], who mistook it for an effect of the increased surface area. Three years later, Jeanmaire and Van Duyne [Jea77] as well as Albrecht and Creighton [Alb77] independently described SERS as the genuinely enhanced process it is. The latter group measured an enhancement factor of approximately 10^5 and already mentioned surface plasmons as a possible explanation.

Nowadays, SERS [Kne99, Hay05, Sti08, Lom08] is explained by the following three enhancing mechanisms:

- An electromagnetic enhancement due to the resonant excitation of localised surface plasmons in the metallic substrate, see chapter 2.2.
- A chemical enhancement due to charge-transfer complexes between the molecules and the substrate [Lom86].
- Resonant excitation in the case of surface-enhanced *resonant* Raman scattering (SERRS).

For the electromagnetic enhancement, the enhancement factor F_{em} at each molecule is approximately given by

$$F_{em} = |F(\omega_0)|^2 \cdot |F(\omega_S)|^2 \ , \tag{2.8}$$

where $F(\omega_0)$ is the local electric-field enhancement factor at the incident frequency ω_0 and $F(\omega_S)$ that at the Stokes-shifted frequency ω_S [Sch06]. Since the plasmon width is often large compared to the Stokes-shift, one can approximate that $F(\omega_0) \approx F(\omega_S)$. Then, equation 2.8 simplifies to

$$F_{em} \approx |F(\omega_0)|^4 \ . \tag{2.9}$$

For a more precise calculation of the electromagnetic enhancement, numerical methods such as the discrete dipole approximation (DDA) and the finite difference time-domain (FDTD) would be necessary.

The second enhancing mechanism is a charge-transfer process between the molecule and the metal substrate. Upon adsorption of a molecule, new electronic states may arise which can serve as resonant intermediate states in Raman scattering

[Cam98]. Often, the highest occupied molecular orbital (HOMO) and lowest unoccupied molecular orbital (LUMO) of the adsorbed molecule are arranged symmetrically above and below the Fermi level of the metal. In this case, charge-transfer excitations can occur either from the metal to the molecule or vice versa. Absorptions from the HOMO to the Fermi level or from the Fermi level to the LUMO then occur at roughly half the energy of the intra-molecular HOMO-LUMO excitation. If the latter is in the near UV range, charge-transfer excitations would be possible in the visible. In short: when a molecule chemically adsorbs onto a surface, its electronic structure can change in a way that leads to surface-enhanced resonance Raman scattering (SERRS).

Up to now, the electromagnetic and the chemical enhancing effect were presented independent of each other. However, they are connected by the fact that the charge-transfer transition moment of the molecular excitation has to be along the direction of maximum amplitude of the plasmonic field, i.e. perpendicular to the metal surface [Lom08]. Then, the most effective Raman enhancement can occur.

Various SERS substrates have been investigated so far. In the visible spectral range, gold, silver or copper are usually used as substrate materials. Additionally, the size and the shape of the plasmonic structures can be varied greatly [Ank08].

2.4.2 Tip-Enhanced Raman Scattering

TERS is a spectroscopic technique established during the last decade [Har08, Dom10]. Similar to SERS, it makes use of the fundamental principle of localised plasmon excitation. The major difference is merely that instead of providing a rough substrate below the molecules, the plasmonic modes are excited in a noble metal tip which approaches the molecules from above. In fact, it has been shown experimentally that the photoluminescence (PL) spectrum of a rough surface and of a tip are indeed similar [Bev03]. The chemical enhancement effect is entirely analogous to the one described for SERS.

TERS makes it possible to study few or even single molecules [Sac08b]. Recently, Steidtner and Pettinger showed measurements of a resonantly excited single brilliant cresyl blue molecule [Ste08].

2.5 State of Research

2.5.1 Fischer Patterns

Fischer patterns are periodic arrays of triangles created by so-called nano-sphere mask lithography [Fis81]. Monodisperse spheres are brought onto a substrate surface

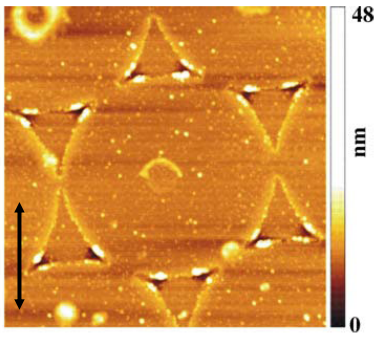

Figure 2.7: AFM measurement of near-field ablation at the tips of Fischer pattern triangles. The black arrow indicates the polarisation direction of a short laser pulse that was used to induce the ablation. Holes and accompanying rims can be seen to have been created by intense near fields in two of the three triangles' corners. Taken from [Bon07].

to form a hexagonally aligned monolayer. Then, a metal film is evaporated on top and reaches the substrate only through the triangular gaps between the nanospheres. After removing these spheres, a pattern of metallic triangles remains: a Fischer pattern.

The evanescent field at the outline of nano-triangles in general has been investigated both directly and indirectly [Lei04, Ran08, Nel10]. Both qualitative and quantitative studies were performed, the latter determining the triangles' near field with high precision in its size and intensity [Gel11, Kol11].

Likewise, the plasmonic behaviour of Fischer patterns has been studied profoundly. Optical extinction spectroscopy [Jen00], confocal microscopy [Gon03] and photopolymerisation [Gel11] all helped to understand their interaction with light.

The group of Leiderer found near-field ablation to be a quite simple yet successful method to investigate the Fischer pattern's near field qualitatively and quantitatively [Lei04, Bon07, Kol11]. They use short (e.g. femtosecond) laser pulses. The strong field enhancement of the optical near field locally ablated the surface around and beneath the triangles. This surface modification was then measured and evaluated by AFM imaging. By initial theoretical calculations, they expected the strongest near-field enhancement at the triangle tips located at the end of the axis parallel to the polarisation of the exciting light (see also [Sch06]). Whereas this proved to be right for smaller triangles, larger triangles showed an optical response turned by 90° with respect to the polarisation direction, as figure 2.7 shows. Kolloch et al. concluded multipole plasmonic modes in the nano-triangles to account for this finding, which was supported by further FDTD simulations [Kol11].

Other research groups found that the material of the triangles plays a distinct role for the Fischer pattern's plasmonic response [Gon03], as do the triangles' edge length and height [Lei04, Jen00, Bon07, Kol11]. Additionally, the dielectric constant of a surrounding liquid [Jen99] and of the supporting substrate [Mal01] can shift the particle plasmon resonance peak. Due to the strong near fields which can arise in Fischer patterns, several research groups have successfully used them as SERS substrates [Hay03, Sti08, Cam08].

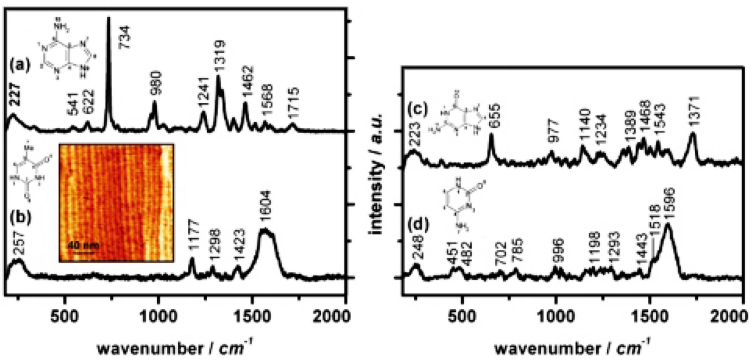

Figure 2.8: TERS measurements of the four DNA bases on smooth gold: (a) adenine, (b) thymine, (c) guanine, (d) cytosine. The inset is an STM image of a thymine self-assembled monolayer. Taken from [Dom07].

However, to my knowledge, no investigations of Fischer patterns by higher order laser modes have been reported so far.

2.5.2 Near-Field Investigations of DNA

The earliest reports of tip-enhanced near-field investigations of DNA still relied on fluorescence for the optical signal [Kim04, Ma06]. However, the advantage of SNOM and TERS is that they allow for the recording of characteristic molecular Raman spectra without labelling.

Rasmussen and Deckert measured the SERS spectra of the four DNA bases on silver island films and TERS spectra of nano-crystalline thymine and cytosine [Ras06]. Later, Domke et al. performed tip-enhanced Raman spectroscopy of all four DNA bases individually on a smooth gold substrate, see figure 2.8 [Dom07]. Their gold SNOM tip is side-illuminated through an objective lens. They use a helium-neon laser at 632.8 nm and an STM system for topographical feedback and imaging. In the case of adenine, they determined to have detected as little as approximately 130 molecules by TERS.

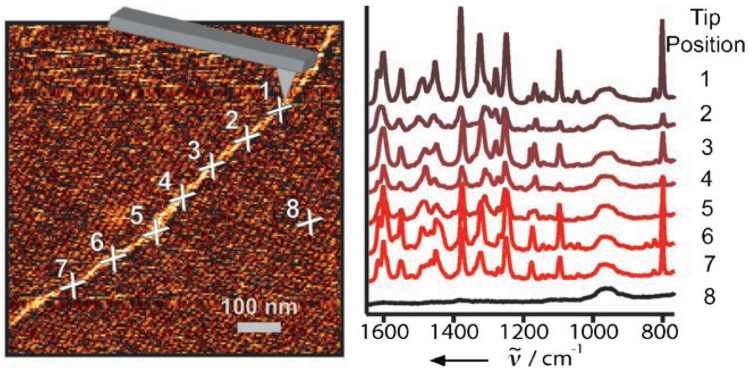

Figure 2.9: TERS measurements along a polycytosine RNA strand. Left, the topographical image with the seven corresponding TERS spectra on the right. An eighth spectrum was taken on the naked mica substrate for reference. Taken from [Bai08].

Shortly thereafter, Bailo and Deckert achieved AFM measurements and accompanying tip-enhanced Raman spectra at specific locations on a poly-cytosine RNA strand, see figure 2.9 [Bai08]. They used a silver coated silicon AFM tip for their measurements and a laser excitation wavelength of 530.9 nm. The tip illumination is achieved from below, i.e. through the transparent mica substrate. Bailo et al. suggest this technique for future sequencing of single natural RNA or DNA strands, emphasising that by measuring the difference between two adjacent spectra it would not be necessary to laterally resolve single bases. They also point out that a stable setup with virtually no lateral sample drift is crucial to the TERS measurements of such a single RNA strand.

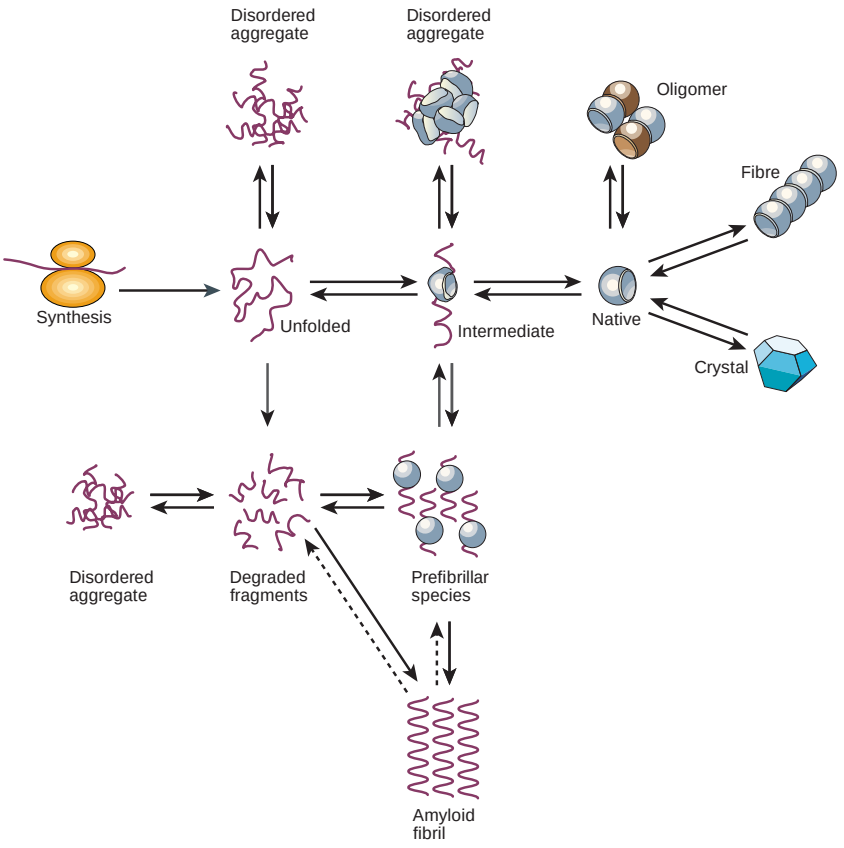

Figure 2.10: An overview of structures that proteins can form. Although the amyloid fibrillar form is just one way of aggregation, it is unique in how highly organised it is. Figure taken from [Dob03].

2.5.3 Raman Spectroscopy of Amyloid Fibrils

Amyloid[5] fibrils are highly ordered aggregates of misfolded proteins [Dob03]. Proteins are long chains of amino acids and can accomplish their biological purposes

[5]The term is owed to Rudolph Virchow's mis-identification of the material as starch, or *amylum* in Latin, in 1854 [Sip00].

only in their natively folded forms. However, as depicted in figure 2.10, on the way from the unfolded to the folded state, a protein can also reach a fibrillar aggregated structure.

As early as 1854, Rudolph Virchow was the first to observe a certain macroscopic abnormality of brain tissue [Sip00]. Only much later it was recognized to contain misfolded fibrillar proteins. In 1944, Waugh observed that insulin forms fibrils when heated and acidificated [Wau44]. Today, several dozens of diseases are known – amongst them Alzheimer's disease and Parkinson's disease – to which amyloid fibrils are indicators.

Recent investigations of amyloid fibrils by Raman spectroscopy include the work of Ortiz et al. [Ort07]. By AFM measurements, they confirmed the formation of fibrils. They performed confocal Raman spectroscopy of both the native and the fibrillar insulin form and calculated difference spectra. By the latter they identified a set of four Raman bands which they interpreted as the Raman signatures of fibrillation.

Almost concurrently, Beier et al. aimed at detecting beta amyloid (β-amyloid) in small quantities [Bei07]. β-amyloid is found in patients with Alzheimer's disease and is believed to play a crucial role in its toxicity. Currently, Alzheimer's disease can only be diagnosed definitively after the patient's death. Beier et al. therefore developed a SERS sensing mechanism based on the plasmonic enhancement of gold nano-shells. With the help of Mie scattering calculations, these nano-shells had been designed to match the setup's laser excitation wavelength. Since β-amyloid shows only weak SERS activity, Beier et al. bound the SERS active dye congo red to it. Hereby they were able to detect β-amyloid in merely picomolar concentrations.

Chou et al. were able to obtain SERS spectra of β-amyloid in a nano-fluidic biosensor [Cho08]. They mixed 60 nm gold nano-particles with the proteins in solution and observed the conformational changes of β-amyloid over time by taking subsequent Raman spectra during the course of five days.

Recently, a first report of TERS measurements on amyloid was published by Deckert-Gaudig et al. [DG10]. They obtained several enhanced Raman spectra of an isolated insulin amyloid fibril. The investigations were done by the research group of Deckert whose measurements on DNA [Bai08] were mentioned in the above section 2.5.2. Again, they propose TERS as a direct sequencing technique for individual amyloid fibrils.

3 The Setup: A Parabolic Mirror Based Scanning Near-Field Optical Microscope

As we have seen in the previous chapter, it is a worthwhile undertaking to reduce the resolution limit of an optical microscope as much as possible. The custom-built setup on which I conducted my measurements achieves this by a unique combination of various features. Its optical path is sketched in figure 3.1. Our setup is operated in ambient conditions: at room temperature (stabilised by air conditioning) and in air.

The optical basis of our setup is a confocal scanning microscope employing a parabolic mirror. The mirror is used both for focusing the incoming laser beam and for col-

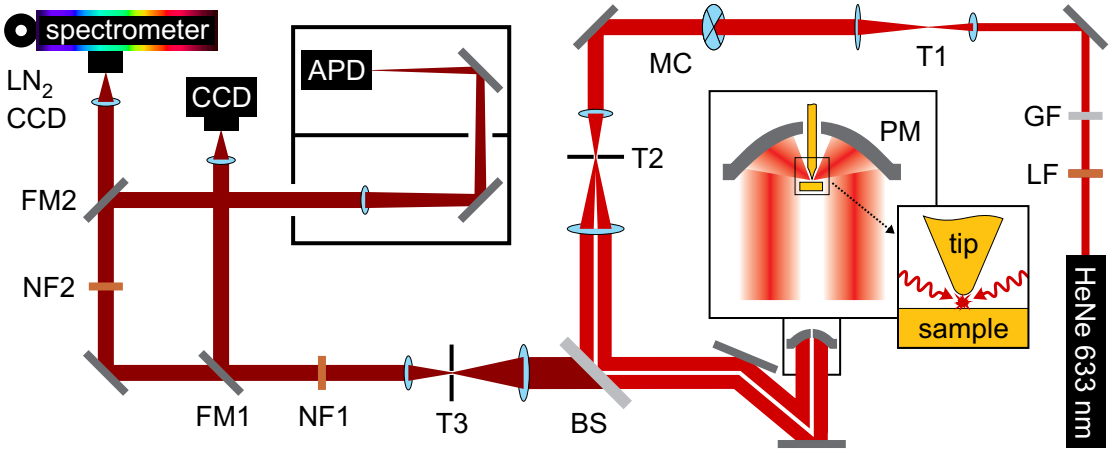

Figure 3.1: Schematics of the optical path of the employed setup. A close-up to the optics inside the parabolic mirror and the excitation of the tip are shown in two subsequent insets. HeNe: helium-neon laser; LF: line-filter; GF: assorted grey-filters, up to an optical density (OD) of 2.5 in steps of 0.5 OD; T: telescope; MC: mode converter; BS: non-polarising beam splitter; PM: parabolic mirror; NF: notch-filter; FM: remotely controlled flipping mirror; APD: avalanche photo-diode; LN_2: liquid nitrogen cooler; CCD: charge-coupled device camera.

lecting the optical response from the sample. It will be addressed in detail in chapter 3.1.1.

A second particularity of the setup is the use of higher order laser modes generated by a mode converter. In combination with the parabolic mirror, they generate intriguing electric field patterns in the focus, as shall be discussed in chapter 3.1.2.

The third noteworthy feature is a sharp gold tip. Put into the laser focus, it acts as an optical antenna and hence a plasmonic source of an intense and highly localised evanescent field. It is employed for scanning near-field optical measurements and tip-enhanced Raman spectroscopy. This part will be elaborated on in chapter 3.2.

3.1 The Confocal Basis

In confocal optical microscopy, a resolution close to the theoretical diffraction limit can be reached. In contrast to classical optical microscopy, the sample area is not illuminated all at once but instead only by the focus of a point light source. To obtain an image, the sample is scanned through the focus – or vice versa the focus is scanned over the sample. In our setup, the former is the case.

The confocal principle is accomplished by using two strategically placed pinholes. If no point light source is employed, a normal light source is focused through a first pinhole and then onto the sample surface. The optical response is then focused through a second pinhole before being led onto a detector. In both cases, the pinhole's purpose is to block all light from beyond the central maximum of the Airy disc (see chapter 2.1). This effectively inhibits emission coming from out of the focus and thus enhances especially the axial resolution. Still, the resolution is diffraction-limited and dominated by the wavelength of the light.

A further gain of confocal microscopy is that it can easily be combined with the spectroscopy of single points on the sample surface.

3.1.1 The Parabolic Mirror

In our setup, we employ a parabolic mirror – see figure 3.2 – both as a laser focusing and as a collecting element for the optical signal. In contrast to lens objectives which have a focal plane, a parabolic mirror has only a focal point and is thus well suited for confocal microscopy. Also, a parabolic mirror yields no chromatic aberration which would occur in a normal lens material.

Most importantly, a parabolic mirror has the highest attainable numerical aperture (NA) in air. Since NA $= n \cdot sin(\theta_{max})$ (see equation 2.1), a lens in air would theoretically have to be infinitely large to reach a θ_{max} of 90° and thus an NA of 1.

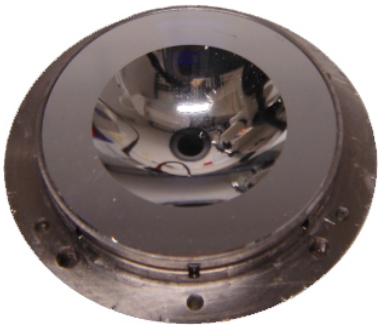

Figure 3.2: Photograph of a parabolic mirror as used in our setup.

A parabolic mirror however can reach this value by covering the whole half-space above the sample. Hence, apart from objective lenses working with immersion oil and thus increasing the refractive index n, a parabolic mirror is an ideal component for increasing the optical resolution of a microscope.

This large angle takes a further positive effect when employing the parabolic mirror as a signal collection element, as we do. Especially when attempting to measure weak optical responses, collecting as much of the signal as possible becomes essential.

However, a parabolic mirror requires attention from the experimenter. If the axis of the incoming light does not hit the mirror perfectly perpendicularly, the mirror will yield a strong comatic aberration [Lie01].

3.1.2 Higher Order Laser Modes

Apart from the standard Gaussian laser mode and the different transverse electromagnetic modes, some intriguing higher order modes can be generated by special mode converters. In combination with a parabolic mirror, they produce particular polarisation orientations in the focus and allow to generate an especially tight focal area.

We use a self-made mode converter assembled from the quarters of two dissected half-wave plates [Sta07]. Starting with a linearly polarised TEM_{00} beam, the polarisation of the light is turned in each segment to face radially outwards/inwards. By focusing through a pinhole, we remove higher spatial frequencies and thus obtain a homogeneously polarised beam. Due to its intensity minimum in the centre of the optical axis, it is called a radially polarised doughnut mode (short: radial mode). Such a radial mode yields a tighter focus [Dor03] and hence a higher optical resolution.

If the same mode converter is turned by 90°, the doughnut mode assumes a polarisation facing azimuthally around the centre of the beam. We then obtain an azimuthally polarised doughnut mode (azimuthal mode).

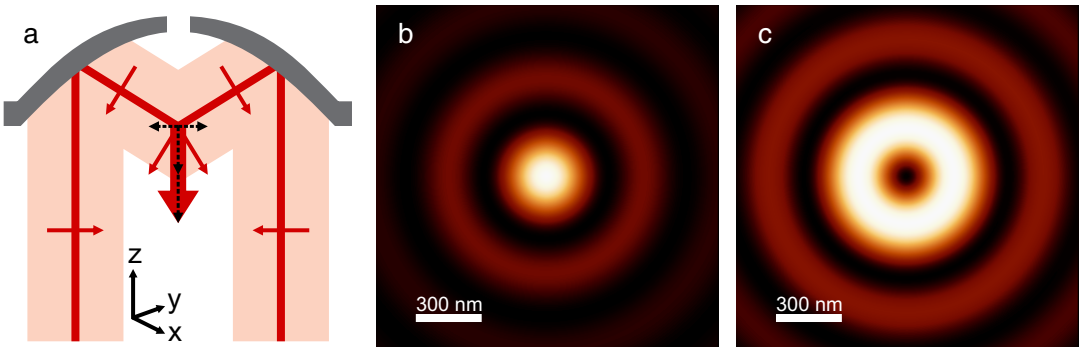

Figure 3.3: Focusing higher order laser modes with a parabolic mirror. (a) A sketch illustrating how a radial mode yields a strongly z-polarised focus. The small red arrows depict the direction of the electric field, the dashed black arrows show their vector components. In the focus, the $\vec{E}$-field components in x and y cancel each other out while the components in z sum up: large red arrow. (b) and (c): Simulation of the free-space field distribution (x, y plane-section) of higher order laser modes focused by a parabolic mirror; laser wavelength $\lambda = 632.8\,\text{nm}$. Computed with PMCalc by Andreas Lieb. (b) Focus of the radial mode. Only $|E_z|^2$, i.e. the electric field intensity normal to the sample surface is depicted; the components parallel to the sample surface are much weaker. (c) Focus of the azimuthal doughnut mode. The total electric field intensity is depicted and corresponds to the field in x and y, since E_z is zero. The field polarisation is azimuthal within the bright focal ring, i.e. parallel to the sample surface.

Focusing a radial mode with a parabolic mirror yields an especially tight focus [Sta08]. Additionally, this focus will have a strong polarisation in z, i.e. along the optical axis and thus perpendicular to the sample surface. This can be illustrated by a simple vector consideration of the electric fields in the focus, see figure 3.3a. Field components in x and y cancel each other out – which is the fundamental reason for the tighter radial focus [Dor03]. Calculations predict for our 632.8 nm laser a focal full width at half maximum (FWHM) as low as 260 nm [Lie01]. Additionally, the strong z-polarisation is crucial for an efficient excitation of the tip in the later described scanning near-field microscopy, see chapter 3.2.3.

Likewise, the azimuthal doughnut mode results in an azimuthal field distribution in the focus, i.e. a polarisation purely in plane with the sample surface. The intensity in the azimuthal focus is ring-shaped with an outer FWHM of 640 nm and an FWHM of the ring itself of 220 nm; figure 3.3c.

3.1.3 Confocal Optical Imaging

In our setup (see figure 3.1), the confocal scanning is done by placing the sample on a scanning stage (517-3CL, Physik Instrumente). Each sample was glued onto a

nickel plate and can thus be attached magnetically to the scanning stage. This is firm enough to prevent sample slips during scanning movements.

Since in our setup the parabolic mirror illuminates the sample from above (see figure 3.1), we can use non-transparent samples. The diameter of our parabolic mirror is approximately 2 cm. It has a small hole in the centre through which a tip can be lowered for topographical and TERS measurements – see chapter 3.2. In order not to block the optical path, we used small samples. Typically, they had an edge length of 5 mm and were glued on round 6 mm diameter nickel plates. Ideally, the sample would be placed entirely in the intensity minimum of the doughnut mode.

Our light source is a helium-neon laser with $\lambda = 632.8\,\text{nm}$ (Melles Griot, 10 mW). The laser excitation power in the confocal focus is 250 µW. The optical response from the sample is collected once more by the parabolic mirror. For easier alignment, our specific mirror has a collection angle of $\theta_{max} = 88.2°$ and hence an NA of 0.9998.

The detection path is separated from the incoming light by a beam splitter and then passes two consecutive notch-filters which block Rayleigh scattered light. In order to map the optical response of the sample while scanning, the signal is then focused onto the tiny active area of an avalanche photo-diode (APD). Its small aperture acts as the second pinhole for achieving confocal resolution as mentioned above. The optical intensity signal is recorded via an XPMPro 1.2.2.1 software.

The observed optical contrast can stem from Raman peak differences or from plasmonic luminescence intensity differences. We use this confocal operating mode to investigate plasmonic sample responses of nano-structured surfaces and to record surface-enhanced Raman scattering. Furthermore, we could conduct fast confocal scans when searching for areas of interest for later near-field investigations.

3.1.4 Measuring Normal and Surface-Enhanced Raman Spectra

By means of an electrically flippable mirror (FM2 in figure 3.1), the optical response of the sample can alternatively be directed onto a spectrometer (SpectraPro 300i, Acton Research). Its CCD camera is cooled by liquid nitrogen to a stable temperature of −80 °C. Spectra were measured with either a 600 or a 150 grooves/mm grating. The spectrometer was regularly calibrated by collecting spectra of silicon which has a characteristic Raman line at $520\,\text{cm}^{-1}$. As a software, WinSpec 2.5.5.1 was employed for the recording of the spectra.

In confocal measurement mode on flat, i.e. non-enhancing substrates, most of the spectra collected during the course of this work showed only the spectrally broad luminescence response of the employed gold substrate. Molecular Raman bands often proved to be too week for detection without an enhancing substrate structure.

By employing either randomly rough gold edges or a periodic array of gold nanotriangles, surface-enhanced Raman bands of molecules became observable.

3.2 The Scanning Near-Field Implementation

In order to further improve the optical resolution beyond the classical diffraction limit, we employ a fine gold tip. Put into the strongly z-polarised focus of the radial mode, it acts as a plasmonic optical antenna – see chapter 2.3. We then scan the sample surface beneath this tip just like in conventional scanning probe microscopy. Hence, the tip simultaneously acts as a topographical feedback element and provides a near-field optical image. It can additionally be employed to collect tip-enhanced Raman spectra at specific points of interest.

3.2.1 Topographical Feedback and Tip Positioning

In standard atomic force microscopy (AFM) [Bin86], the forces between a fine tip and a sample surface are determined by measuring the vertical bending of a flexible cantilever. However, the advisable scanning mode for sensitive samples is the so-called intermittent contact mode (also called dynamic contact mode or tapping mode) where the tip vibrates vertically. In our case, we have several reasons not to work with intermittent contact mode: the first is that the tip would constantly move in and out of the near field region. Secondly, gold is too soft a material to withstand such an intermittent sample contact without a deformation of the tip apex. And finally, an AFM cantilever would be geometrically incompatible with a parabolic mirror.

We therefore use a shear-force feedback system based on the resonance of a small quartz tuning fork [Kar95]. The tuning fork is approximately 3 mm in length. It is mechanically excited to vibrate at its native resonance frequency (around 31000 kHz) via the electric excitation of a piezo tube, see figure 3.4. A lock-in amplifier (Ametek Signal Recovery 7270 DSP) provides the excitation and read out of the vibration. A gold tip is glued to one of the tuning fork's prongs in a way that the tip apex would be the first point to touch the sample surface. The coarse-positioning of the tip into the focus is done via a self-built tip runner. By slip-stick motion steps of piezo stacks, it moves the tuning fork in all three spatial directions. For the fine positioning of the tip, the above mentioned piezo tube is again made use of.

To guarantee the necessary stability, the whole setup is mounted on a passively and actively damping optical table (Newport RS 4000). The distance between the tip apex and the sample surface is determined by the Ametek lock-in amplifier

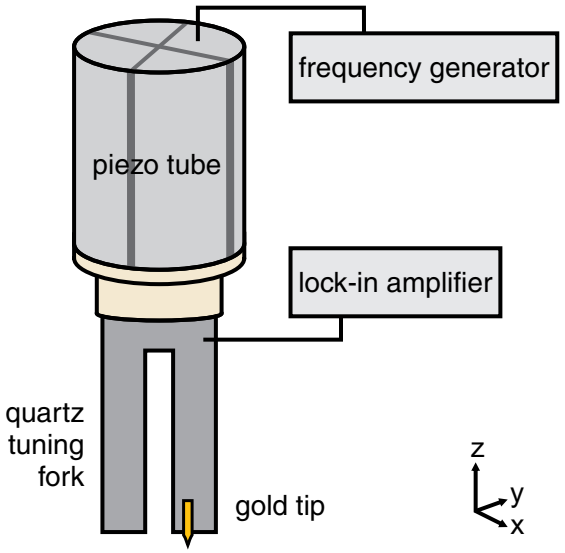

Figure 3.4: Sketch of the setup unit ensuring the topographical feedback. The shear-force between the tip and the sample results in a measurable damping and frequency-shift of the vibrating quartz tuning fork.

measuring the vibration of the tuning fork via the piezo-electric effect of its quartz material. Upon approaching the sample, the free resonance frequency will shift and the oscillation amplitude will be dampened. Both of these effects are taken into account by the feedback system [Bra07]. For our scanning measurements, we usually adjust the setpoint to a phase-shift of 5°. The phase-shift is a relative measure for the tip-sample distance [Sac08a]: a higher setpoint indicates a smaller tip-sample gap. As an absolute value, it is subject to the materials of the two [Bra07] and also depends on the general hardware configuration. For a gold tip above a gold substrate, 5° proved to be a good trade-off between a narrow gap (see chapter 2.3) and still keeping the tip at a safe distance from the sample. This way, we achieve reasonably fast scanning speeds.

The lateral vibration of the tuning fork prongs and hence of the gold tip is merely in the order of ångströms, thus keeping the tip apex inside the 260 nm laser focus. Also, in order to maintain the tip-sample distance constant, the sample was correspondingly moved up and down during the scan. This is especially important when working with near-field optics since the strength of the exponentially decaying evanescent field is extremely sensitive to this distance, see chapter 2.3. Setting the electronics to a constant phase-shift – the analogy to a constant force mode in AFM – is the best option to minimise artefacts in the optical signal. In our setup, the electronic feedback was accomplished by an SPM 1000, RHK Technology. The corresponding software XPMPro was used to record and visualise the images.

In later experiments, the setup was extended to also comprise the possibility to use a tunnelling current as the feedback variable in the way of scanning tunnelling microscopy (STM) [Bin82]. Since the same tip runner was employed in those exper-

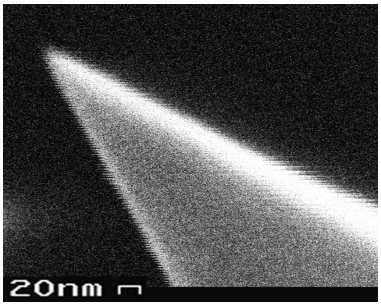

Figure 3.5: SEM image of a good gold tip created by HCl etching.

iments, the tuning fork was still the support of the gold tip but was not excited to vibrate.

3.2.2 Tip Fabrication

We produce our gold tips by electrochemical etching of a 100 µm gold wire (ChemPur) in concentrated hydrochloric acid solution (HCl 37 %) [Böh07]. A platinum wire counter electrode was placed incide the acid, roughly 1 cm below the meniscus of the HCl forming at the gold wire. Rectangular voltage pulses of 8 V and 33 µs duration were applied at a repetition rate of roughly 4.5 kHz, until all the gold in the solution was etched away and a tip formed at the meniscus. All of the tips were characterised by scanning electron microscopy (SEM; Zeiss DSM 962) and only the best ones used in measurements. We aimed for a symmetric and smooth conic shape and an apex diameter of 10 to 20 nm, such as with the tip shown in figure 3.5.

3.2.3 Near-Field Optical Imaging

When employing the gold tip not only as a topographical feedback probe but additionally as an optical antenna, we work in radial laser mode. As was discussed in chapter 2.3, its strong z-polarisation in the focus optimally excites the plasmons responsible for the strong evanescent field at the tip apex.

This nano-scale near-field region then determines the optical resolution of our SNOM. Similar to the parabolic mirror which serves both as optical focusing and collecting element, the tip acts as an antenna focusing the electromagnetic intensity into the near-field region and also collecting optical signals from this region by coupling them back into the tip.

Thus, a two way enhancement of the optical signal can be achieved. This has previously been observed in our lab, when a photoluminescence (PL) enhancement by a factor of $6 \cdot 10^5$ was detected on molecular edges of a diindenoperylene (DIP) film [Zha10]. The measured optical resolution had been 17 nm and it was concluded

that the PL contrast resulted from the local film morphology via a strong coupling between the tip plasmons and exciton-polaritons in the DIP film. The excitation enhancement was found to be $4 \cdot 10^4$-fold and the collection enhancement 15-fold.

In our scanning near-field measurements, topography as well as optical contrast were collected simultaneously by the XPMPro software.

3.2.4 Measuring Tip-Enhanced Raman Spectra

Areas of interest for TERS measurements were chosen either from the topographical or from the corresponding near-field optical image. To actually detect tip-enhanced Raman bands, the tip-sample gap has to be further diminished by increasing the setpoint of the shear-force feedback (see chapter 3.2.1). Only below a certain gap size, TERS spectra became observable.

In order to determine the TERS enhancement factor F_{enh} experimentally, the intensity of a TERS band has to be compared to that of the same band collected at the same spot without tip enhancement, e.g. in normal confocal far-field mode. In the case of a flat substrate which on its own yields no enhancement and furthermore assuming a small amount of molecules is dispersed on the surface, the straight forward enhancement is $F_1 = I_{nearf}/I_{farf}$. Here, I is the intensity of a specific Raman band as rising above the PL background, measured in far field ($farf$) or by the near field ($nearf$) of the tip.

However, we also have to take into account that the near field region is much smaller than the confocal focus. Hence, the measured TERS signal originates from far less molecules. This implies an additional enhancement. Presuming a uniform surface coverage with Raman active molecules, it is given by $F_2 = A_{farf}/A_{nearf}$, where A is the FWHM area illuminated either confocally or by the near field.

We determine A_{nearf} via the FWHM of the smallest topographical features observed in measurements with the same tip. Since the topography is a convolution of the tip apex size and the actual structure of the surface, the smallest features in topographical images give us an idea of the shape of the tip apex and hence of the near-field size.

Thus, the total TERS enhancement factor [Fle08] can be calculated by

$$F_{enh} = \frac{I_{nearf} \cdot A_{farf}}{I_{farf} \cdot A_{nearf}} \,, \tag{3.1}$$

As stated in chapter 3.1.4, normal confocal spectra of molecules seldom yielded detectable Raman bands. We concluded that in these cases the intensity of the

spectral peaks was below the noise of the measurement. Then, we could only measure this noise as an upper limit for I_{farf}. This gave us a lower limit for the enhancement factor F_{enh}. The real enhancement may be several orders of magnitude higher.

3.3 Typical Experimental Routine

Day-to-Day Alignments

Some slight optical readjustments have to be performed at the beginning or each measurement day: the doughnut mode has to be checked and corrected, the beam has to be made to hit the parabolic mirror exactly perpendicularly and the collected signal has to be centred onto the small aperture of the APD – compare figure 3.1 on page 21.

After a warm-up period of the laser, the first task is to adjust the doughnut mode. Mostly, this can be achieved solely by fine positioning the pinhole in the focus of the telescope T2. Seldom, the mode converter has to be readjusted additionally.

Due to the large collection angle of the parabolic mirror, the sample sits almost inside its curvature (see inset in figure 3.1). Hence, the parabolic mirror has to be removed when inserting the sample. After placing the mirror back, the sample is moved into the focus in z by observing the optical pattern on the CCD camera. With the help of an extra camera which looks at the sample from above and through the small hole in the mirror, we furthermore ensure that the focus is placed approximately on the centre of the sample surface. Thus, the sample should fit into the central minimum of the doughnut mode and cut off as little as possible both of the laser beam and of the stray light coming from the sample.

Finally, the penultimate mirror in front of the APD is aligned for a maximal APD signal. As explained above, only then the confocal principle is ensured.

Confocal Measurements

Now, confocal sample scans can be performed and confocal Raman spectra can be collected. This is either an end in itself – e.g. to image plasmonic luminescence patterns or for SERS measurements – or can be used to find areas of interest for a later close-up by SNOM.

Near-Field Measurements

When we employ a tip for near-field measurements, only the radial doughnut mode is used, since an $\vec{E}$-field excitation along the tip axis is necessary in order to efficiently

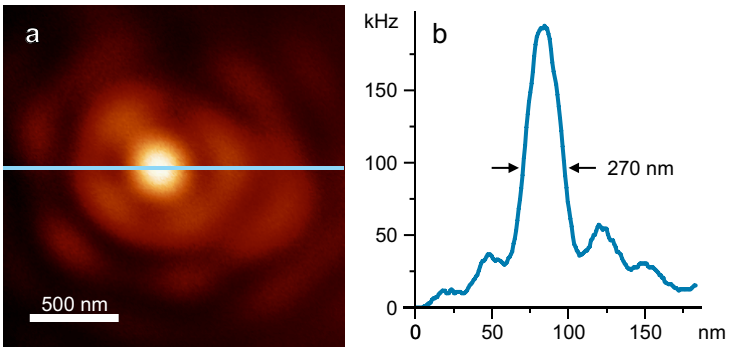

Figure 3.6: (a) Optical image when scanning the tip through the focus of the radial mode. (b) The corresponding intensity profile after a slight smoothing by WSxM. The intensity is given in kilo Hertz, standing for kilo counts per second.

excite the tip (see chapter 2.3). The tip runner is placed on the stainless steel plate that also supports the parabolic mirror. Using its coarse-positioning, the tuning fork is carefully driven downwards through the central hole of the parabolic mirror. Lowering the sample out of the focus and placing the extra camera horizontally next to the sample stage, we observe the tuning fork entering the focal area.

After coarse-positioning the tip in the focal area, we perform a tip scan through the focus. This way, we find the exact position of the tip in the focal maximum. With a fine, symmetric tip, such a scan should essentially map the intensity distribution in the radial focus as calculated in figure 3.3b. This reasoning is supported by our experiments: with a well adjusted focus, we recorded optical images as the one shown in figure 3.6. By measuring several such images with different gold tips, I found the FWHM of the focal intensity to be (265 ± 20) nm. This reproduces well the theoretically predicted 260 nm stated in chapter 3.1.2. It is also noteworthy that 265 nm is distinctly smaller than half of the employed wavelength of our 632.8 nm helium-neon laser.

As the tip heats up in the laser focus, the tuning fork's free resonance frequency will slightly detune. Hence, before approaching the sample to the tip, we need to wait for this frequency to settle. Only then we start moving the sample up stepwise, always checking with the RHK approach motor for a feedback contact between tip and sample. When this is established, we can start scanning the sample beneath the tip and through the focus. An example of such a simultaneous recording of topography and corresponding near-field optical signal is depicted in figure 3.7.

Collecting Tip-Enhanced Raman Spectra

With the XPMPro software, the tip was moved to a specific spot of interest detected either in the topographical or in the near-field optical image. The second flipping mirror (FM2 in figure 3.1) was then lowered, its electronics being smooth enough not to induce vibrations which might damage the gold tip. At this point, the tip was still in a 5° phase-shift feedback contact with the sample. In the experiments described in this thesis, working with a gold tip above gold substrates, the thereby

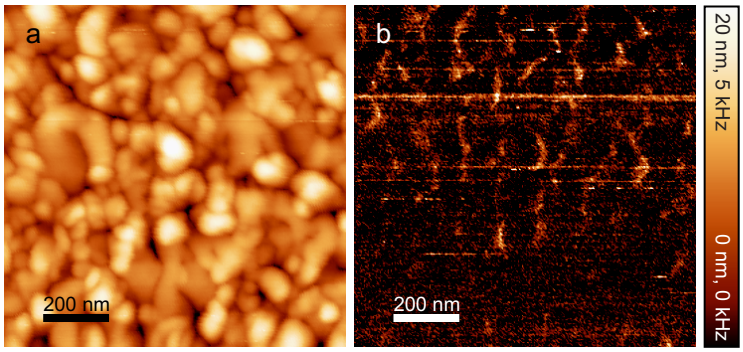

Figure 3.7: Sample scanning: (a) shear-force topographical and (b) simultaneously recorded near-field optical image of an evaporated gold surface. A 1 OD grey-filter had been placed behind the laser during this measurement.

determined gap size proved to be still too large to observe Raman bands of molecules. Therefore, the further proceeding was to collect a series of spectra whilst in between successively increasing the feedback setpoint. During such a stepwise approach of the tip to the sample, we often observed a spectral red-shift of the maximum of the gold luminescence. This was followed by a sudden appearance of strong Raman lines. For a gold tip and a gold substrate, this generally happened at setpoints between 15° and 20° phase-shift.

Tip-Scanning Mode

An alternative mode of operation is to scan the tip instead of the sample. The resulting topographical image will be generated analogously to the case of the sample scan. The optical image collected with the APD however will show the focus similarly to figure 3.6a, with additional features due to the structures on the sample. An example of the tip-scanning mode is shown in figure 3.8.

When working in this operation mode, TERS spectra could only be collected within the bright maximum of the optical image, i.e. when placing the tip in the centre of the focus. Still, if the molecules or structures under investigation covered most of the surface, this approach proved to be a beneficial option since it is immune to slight drifts of the tip out of the previously determined focal maximum.

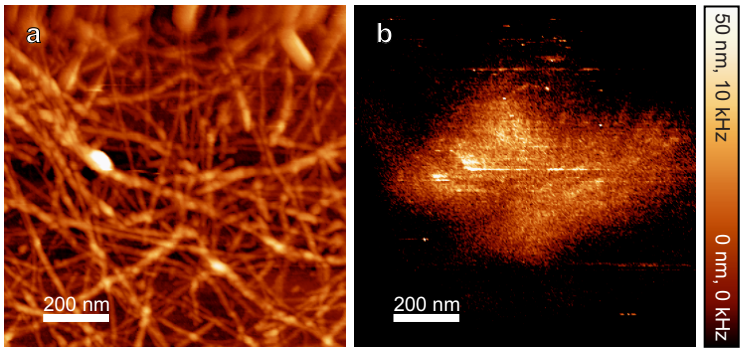

Figure 3.8: Tip scanning: (a) shear-force topographical and (b) simultaneously recorded near-field optical image of amyloid fibrils on a flat gold surface.

Data Analysis

The collected data was analysed and carefully edited with different software programs: the topographical and optical contrast images collected with XPMPro were processed with WSxM [Hor07]. If not indicated otherwise, the topographical images were flattened by an offset or a slope and the contrast slightly adjusted for clarity. Optical images were likewise adjustment in contrast. In the case of the confocal scans of Fischer patterns (chapter 4.3), obviously discordant bright lines or line parts appearing in the fast scan direction were removed in the WSxM software by interpolation of adjacent lines. WSxM also allowed to make line-sections across the topographical or optical images in order to determine a height profile or an intensity distribution respectively. I performed one smoothing step in WSxM on these line-section profiles. The spectra collected with WinSpec were converted to raw data with MagicSERS (by Marcus Sackrow) and then plotted for presentation using OriginPro.

4 Plasmonics of Gold Fischer Patterns

Fischer patterns are periodic arrays of metal nano-triangles that can easily be created by mask lithography (see following section) [Fis81]. Being metal nano-particles, plasmonic modes can be excited inside the triangles. In this chapter, I report on the confocal investigation of gold Fischer patterns with the previously introduced higher order laser modes.

A strong dependence of the location of 'hot spots' in Fischer patterns on the polarisation of the incident light had been determined previously [Bon07]. However, such experiments had worked with light polarisations in the surface plane only. In our setup, we can tune the polarisation in our focus to be either in plane by using the azimuthal mode or perpendicular to the sample surface by switching to the radial mode - see chapter 3.1.2.

With these higher order laser modes, we expected to pointedly excite specific particle plasmon modes in the nano-triangles. The locations of ideal plasmonic excitation would then be detected as strong far-field luminescence by our setup in confocal scanning mode.

The work on Fischer patterns [Fis81] as presented in this chapter was a collaboration with Andreas Kolloch from the research group of Professor Leiderer at the University of Konstanz. The group has many years of experience in investigating Fischer patterns [Lei04, Bon07, KB07, Kol11].

4.1 Sample Preparation

We provided square 5 mm edge length substrates of silicon or glass to Andreas Kolloch. The substrates had been cut by a wafer saw from commercial silicon wafers and commercial glass slides (Menzel-Gläser) respectively. All the samples were then prepared by Andreas Kolloch via colloid lithography. First, a self-assembled monolayer of polystyrene spheres was deposited on a substrate piece via drying of a strongly diluted colloidal suspension [Bur97]. The colloids form a tightly packed hexagonal

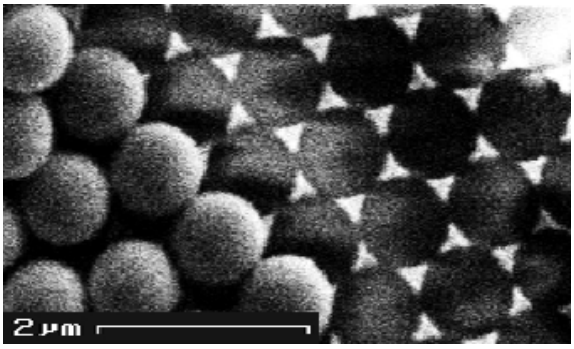

Figure 4.1: SEM image of a Fischer pattern with the polystyrene bead mask only partially removed.

lattice with small triangular gaps between them. Subsequently, a thin gold film was evaporated on top in a Bal-Tec BAE 250 evaporating machine. This way, the polystyrene colloids acted as a mask on the respective substrate, allowing the gold to reach the surface merely through the triangular gaps. Only shortly before the first measurement, the colloids were removed in our lab with adhesive tape.

The resulting sample is a regular array of gold nano-triangles on the substrate, often referred to as a Fischer pattern. The scanning electron microscopy (SEM) image in figure 4.1 depicts a sample where the beads are partly removed, showing both the mask monolayer and the resulting Fischer pattern.

Polystyrene spheres of diameters D between 200 nm and 1500 nm were used. The film height h of the evaporated gold was varied between 40 nm and 200 nm. See figure 4.2 for the denominations of the triangle dimensions. Not all combinations of sphere size and film thickness could be produced since the film thickness has to be distinctly smaller than the polystyrene sphere radius in order to obtain flat nano-triangles.

For SERS investigations on these Fischer patterns, I prepared a solution of 10^{-6} M adenine monomers (Sigma-Aldrich) in triple distilled water. I put a 30 µl droplet of this solution onto the substrate and after one hour of incubation gently soaked it off with a lint-free tissue, taking care not to touch the sample. The low concentration of the solution was chosen in order to obtain a monolayer or less coverage of adenine on the surface.

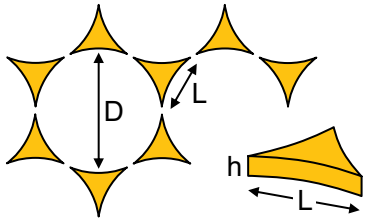

Figure 4.2: Sketch explaining the denominations used to describe the gold nano-triangles of our Fischer patterns. D is the diameter of the employed polystyrene spheres, L the edge length of the resulting triangles; h stands for the height of the evaporated gold film and hence of the nano-triangles.

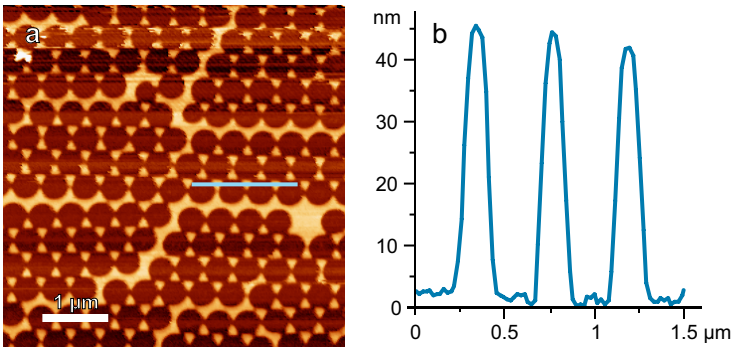

Figure 4.3: Shear-force topographical measurement of a gold Fischer pattern evaporated on a silicon substrate. The evaporation height had been $h = 40\,\text{nm}$ and the employed bead diameter $D = 400\,\text{nm}$.

4.2 Topographical Investigations

I investigated some of the Fischer pattern samples topographically employing our shear-force setup in sample scanning mode, see chapter 3.2.1. One such measurement is depicted in figure 4.3.

I observed well aligned nano-triangles interrupted by slightly larger gold structures. The latter result from dislocations within the self-assembled monolayer of the polystyrene mask. This is a problem which to my knowledge all researchers working with Fischer patterns encounter [Bur97, Gon03, Bon07]. I found the triangles to have an edge length L (see figure 4.2) of approximately 80 % of a sixth of the circumference of the spheres used: $L \approx 0.8 \cdot 1/6 \cdot \pi D$. This same relation had previously been observed by Goncalves [Gon03].

4.3 Confocal Investigations

4.3.1 Fischer Patterns on Silicon Excited by Radial Polarisation

Almost all of the flat ($h = 40\,\text{nm}$, figure 4.4a-d) nano-triangles on silicon yielded an extremely weak luminescence contrast. In radial mode, the triangles with $L \approx 170\,\text{nm}$ (figure 4.4b) were the only ones to show a clear pattern. Here, the bright spots had an average intensity of roughly 5 kHz, i.e. 5,000 counts per second. Due to their hexagonal layout and inter-distance, it is very probable that each of the bright spots marked the centre of a former bead position.

The higher triangles with $h = 200\,\text{nm}$ yielded clearer contrasts. The Fischer pattern with $L \approx 350\,\text{nm}$ showed bright spots of triangular shape (figure 4.4e). These had to be located at the same places as the gold nano-triangles. However, their orientation was turned by 60° with respect to that of the gold triangles.

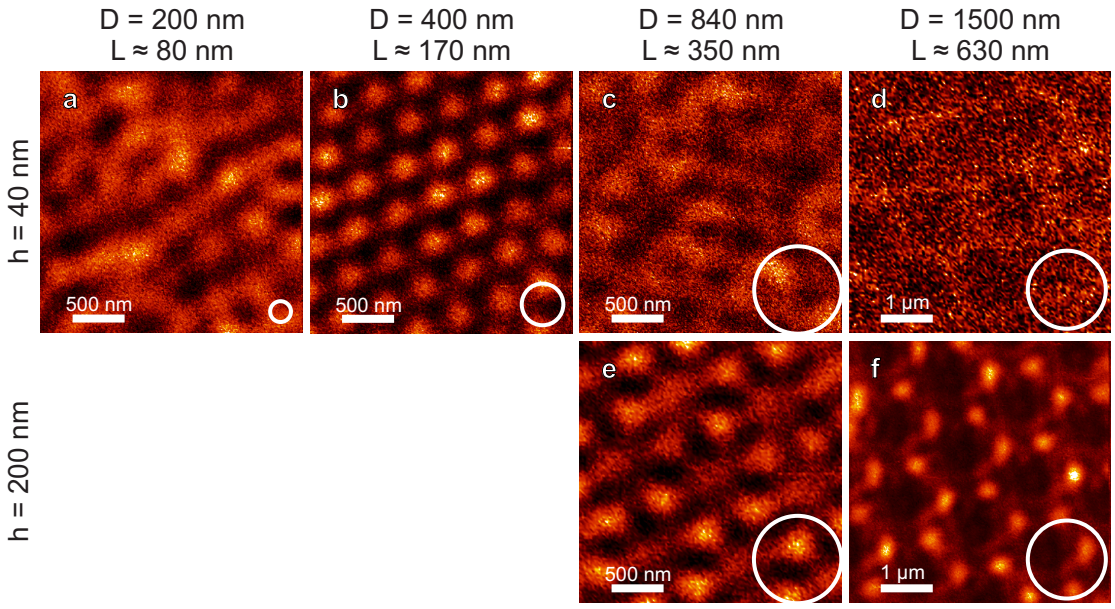

Figure 4.4: Confocal luminescence images of gold Fischer patterns on a silicon substrate. The images were recorded by scanning in radial laser mode. For a visualisation of the employed bead size, their respective outline is sketched in the corner of each image. However, its position does *not* correspond to a probable former bead position. Note the twice as large dimension of images (d) and (f).

Eventually, the largest high triangles ($h = 200\,\text{nm}$, $L \approx 630\,\text{nm}$, figure 4.4f) showed a regular pattern of bright dots with some additional structures in-between. Each bright spot can be assigned quite straightforwardly to the location of a gold triangle. The first maximum ring of the radial focal intensity (see figure 3.3b on page 24) is very likely to be the cause of these additional luminescence structures.

4.3.2 Fischer Patterns on Silicon Excited by Azimuthal Polarisation

In azimuthal doughnut mode illumination, the flat nano-triangles with $h = 40\,\text{nm}$ (figure 4.5a-d) showed the same weak contrast as they had in radial mode. Only with the largest triangles ($L \approx 630\,\text{nm}$, figure 4.5d) a very faint but regular hexagonal mesh was distinguished. The slightly brighter areas can be assigned to the gold triangles and the regions between two adjacent triangle tips.

The higher triangles with $h = 200\,\text{nm}$ again showed clearer images. With the Fischer patterns of $L \approx 350\,\text{nm}$ (figure 4.5e), the confocal image showed a periodic structure. Its reoccurring sub-pattern resembled bright rods aligned to each other like the edges

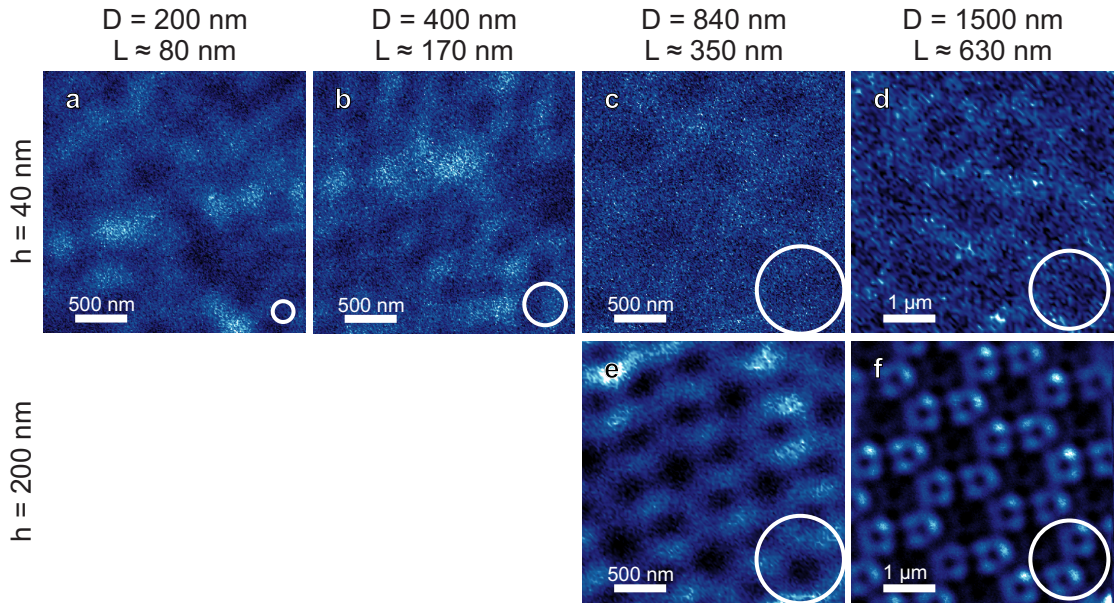

Figure 4.5: Confocal luminescence patterns of gold nano-triangles on silicon obtained by scanning through the azimuthal laser mode. Note the larger scale of (d) and (f).

of a triangle. By comparing this luminescence structure to the most probable former position of the polystyrene beads, I found that each of these luminescing triangles was rotated by 60° against an actual gold triangle.

Finally, the largest triangles with $h = 200\,\text{nm}$, $L \approx 630\,\text{nm}$ showed a regular pattern of bright hollow triangles (figure 4.5f). These luminescence structures were smeared out to resemble squares, which was probably due to a slight misalignment of the optical path [Lie01]. The brightest spots were all located in the middle of the gold triangles' edges. At this point, an allocation of where these luminescence maxima actually stem from can hardly be given, due to the complex focal intensity distribution of the azimuthal laser mode, recall figure 3.3c.

4.3.3 Fischer Patterns on Glass Excited by Radial Polarisation

In both higher order laser modes, Fisher patterns on glass (figures 4.6 and 4.7) yielded a significantly stronger luminescence and a higher contrast than the triangles on silicon. Therefore, the observed luminescence patterns can be discussed in greater detail. The patterns varied considerably both with the edge length L and with the height h of the nano-triangles.

Regarding specifically the investigation in radial laser mode, just like on silicon, with the small triangles ($h = 40\,\text{nm}$ and $L \approx 80\,\text{nm}$, figure 4.6a), it was not possible to

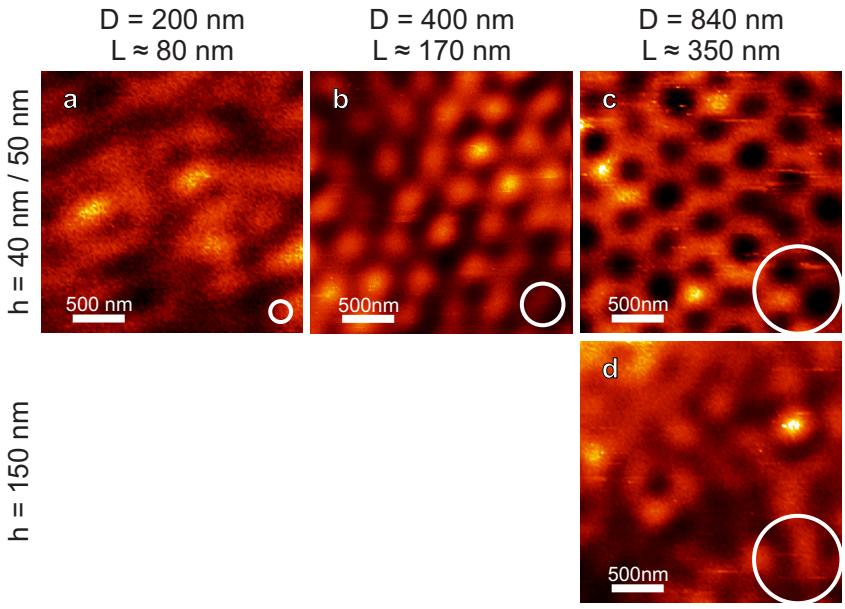

Figure 4.6: Confocal luminescence patterns of gold nano-triangles on glass measured in radial laser mode. In (a) and (b) the height of the triangles was $h = 40\,\text{nm}$, whereas in (c) it was $h = 50\,\text{nm}$. Again, the outline of the respective bead size is sketched in each image corner for a size comparison.

recognize a regular pattern. This could be due either to a poorly aligned monolayer of the small $D = 200\,\text{nm}$ polystyrene spheres used. Moreover, our focal size of 260 nm is much larger than these triangles and hence cannot resolve them. It is conceivable that the luminescence contrast depicted in this case was mostly due to imperfections in the Fischer pattern.

The medium sized triangles ($h = 40\,\text{nm}$, $L \approx 170\,\text{nm}$, figure 4.6b) showed a hexagonal pattern of bright dots which on average had an intensity of approximately 60 kHz (60,000 counts per second). The pattern resembled very much that of the gold triangles on silicon (figure 4.4b). Like there, it seems that each bright dot marks the former centre of a polystyrene sphere.

The large, flat triangles ($h = 50\,\text{nm}$, $L \approx 350\,\text{nm}$, figure 4.6c) yielded a honeycomb structure of hexagonally connected lines. Taking a closer look, every second dark spot in a row was slightly larger than the others. These larger dark areas had an overlying hexagonal alignment. They had a mean distance of approximately 870 nm. Even though this is 4 % more than the denoted polystyrene sphere size of $D = 840\,\text{nm}$, the only conceivable alignment to match this pattern is that these darkest spots mark the former sphere positions. Slight misalignments – as also

observed topographically (see figure 4.3) – will always lead to a larger mean distance of their positions.

Provided these larger dark areas are the former bead positions, I deduce from figure 4.6c that each gold triangle yielded a bright threefold star where the beams were directed towards the edges of the triangle. The secondary dark areas were then located between two adjacent gold triangle tips. This can be explained by a bright luminescence stemming from the centre of the nano-triangle by means of a plasmonic centre mode and additional enhanced luminescence at the middle of the triangle edges caused by an edge mode [Nel10]. These are particle plasmon modes: eigenmodes of plasmonic enhancement. They are dubbed according to the spots where they generate a strong field enhancement. This near field radiates into the far field which is the luminescence we then observe. However, no definite comparison to other works with Fischer patterns can be made since no other report of nano-triangle investigations by z-polarised light is known to me.

When scanning thicker triangles ($h = 150\,\mathrm{nm}$) of the same edge length $L \approx 350\,\mathrm{nm}$ (figure 4.6d), no conclusive optical pattern could be observed, although I attempted this at several different sample areas. The reason may again have been a difficulty in obtaining a perfect self-assembled monolayer of polystyrene spheres, but it is also possible that this gold film was already too thick to yield flat triangles and possibly agglutinated the spheres.

4.3.4 Fischer Patterns on Glass Excited by Azimuthal Polarisation

With the azimuthal laser mode (figure 4.7), I partially observed different luminescence patterns than in radial mode. The smallest triangles again showed no regularity in the intensity pattern (figure 4.7a).

The medium sized triangles (figure 4.7b) yielded a pattern of bright dots very similar to the investigation by radial laser mode. In fact, when scanning the same area consecutively with radial and azimuthal mode, it became evident that in both cases the exact same locations showed luminescence maxima. This is surprising, since we have to bear in mind the different focal patters – see figure 3.3. In contrast to radial mode, a bright spot in azimuthal mode is actually not located where it appears to be but somewhere in a radius of 530 nm next to it, considering the azimuthal focus has an intensity *minimum* in the centre.

The large, flat triangles again showed the most distinct pattern (figure 4.7c). This is not surprising, since the resolution gets better the lager the depicted features are with respect to the focus size. I now observed a pattern of weakly connected bright

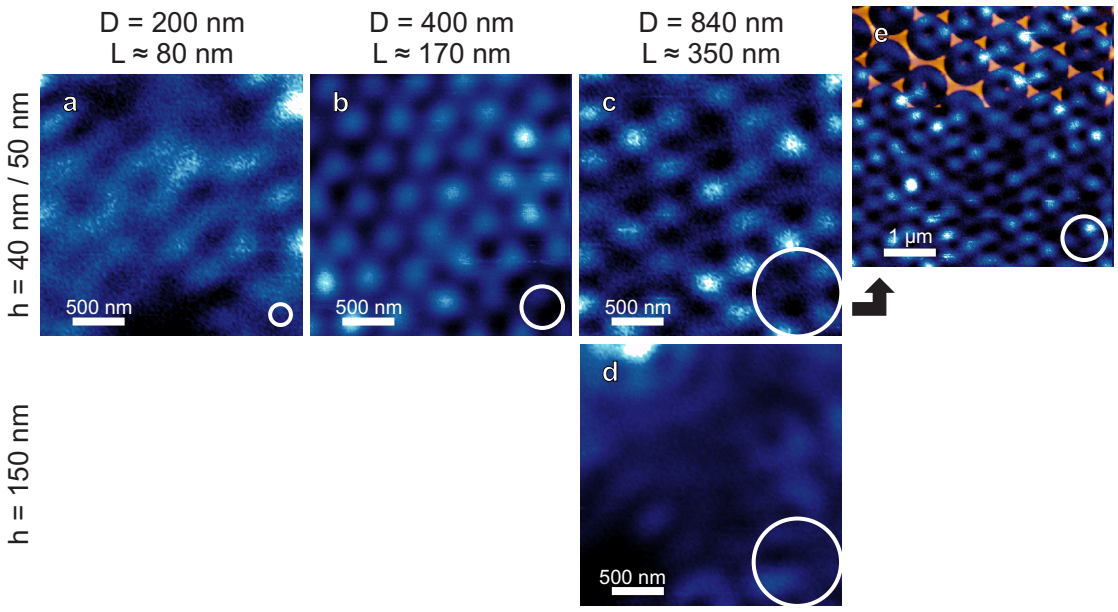

Figure 4.7: Confocal luminescence patterns of gold nano-triangles on glass by azimuthal laser mode scanning. Again, in (a) and (b) $h = 40\,\text{nm}$, whereas in (c) and (e) $h = 50\,\text{nm}$. (e) was performed on the same sample as (c) and is an overlay of a topographical shear-force measurement and a subsequent confocal measurement. Note that image (e) depicts a larger scan area.

dots. Again, every second dark area was slightly larger, probably marking a former sphere position.

Additionally, I placed our shear-force tip in the centre of the azimuthal focus and performed a topographical scan on this sample directly after a confocal measurement. Since the azimuthal focus is isotropic in x and y, the luminescence pattern cannot affect the three gold triangle tips in different ways. However, in the overlay of topographical and confocal measurement (figure 4.7e), this seems to be the case. I conclude that the tip had been shifted slightly with respect to the centre of the azimuthal focus.

Nevertheless, we learn something else from this overlay: larger gold structures (as resulting from misalignments in the polystyrene monolayer) yield areas of weaker confocal signal. I confirmed this by observations in many further measurements both in radial and in azimuthal mode. This proves that the here collected confocal luminescence patterns depict particle plasmon enhancements. In larger gold areas, such particle plasmon modes cannot be excited in the same way.

Just as in radial investigation mode, the thick, large triangles (figure 4.7d), gave no regular optical pattern.

As a first conclusion, I found that the gold Fischer patterns on glass yielded luminescence patterns which were very different from those of the triangles on a silicon substrate. The contrast and luminescence intensity were considerably higher on glass. Only the patterns of the $h = 40\,\text{nm}$, $L \approx 170\,\text{nm}$ triangles led to resembling intensity patterns on silicon and glass: compare figure 4.4b to figure 4.6b.

Recalling the Mie theory discussed in chapter 2.2, we note that the dielectric constant of the medium surrounding the metal nano-particle plays a crucial role in describing its plasmonic resonances. Here, we have a slightly more complicated situation where the particle is flanked by a different medium on each side: air above and silicon or glass below it. Nevertheless, the substrate material will have an influence. In the case of silicon and glass, the respective dielectric constants vary considerably: while that of glass is roughly $\epsilon_{glass} \approx 2.3$, the dielectric constant of crystalline silicon is as high as $\epsilon_{Si} = 15$ [Pal98]. This great difference can undoubtedly be held accountable for the observed deviation in the plasmonic responses on these two substrates.

We need to bear in mind that silicon forms a natural glass-like oxide layer SiO_x on its surface. Still, this layer is extremely thin (in the order of 20 Å [Boy82]) compared to the triangle's near field, which is some tens of nanometres in size. We can hence assume the high dielectric constant of the pure silicon to be mainly responsible for our observations.

4.3.5 Comparison with a Theoretical Convolution Solution

In order to further understand the experimental findings, Josip Mihaljevic performed theoretical calculations of how the gold triangles would simply reflect the laser light. He computed a convolution of the Fischer patterns and the focal intensity distribution as it was depicted in figure 3.3. This was done both for the radial and for the azimuthal focal intensity. However, the actual light polarisation in the focus was ignored. Likewise, the thickness of the gold film and the material of the substrate were disregarded. Most importantly, possible plasmonic excitations were also neglected by this theory. These calculated intensity patterns are shown in figure 4.8.

When comparing the experimentally obtained luminescence patterns of gold nanotriangles on silicon (figures 4.4 and 4.5) to the theoretical convolution images, I found many matches. As stated before, the flat triangles with $h = 40\,\text{nm}$ had yielded scarce contrast and are hence not comparable to the computed patterns. The triangles with $h = 40\,\text{nm}$, $L \approx 170\,\text{nm}$ being the only exception showed a different pattern than the theory. However, the luminescence patterns of all four investigated Fischer patterns with $h = 200\,\text{nm}$ were reproduced accurately by the calculations. This means that the measured luminescence in these cases does not necessarily need plasmonic effects to be understood. It may already be explainable by simple scattering of the light on the gold surface.

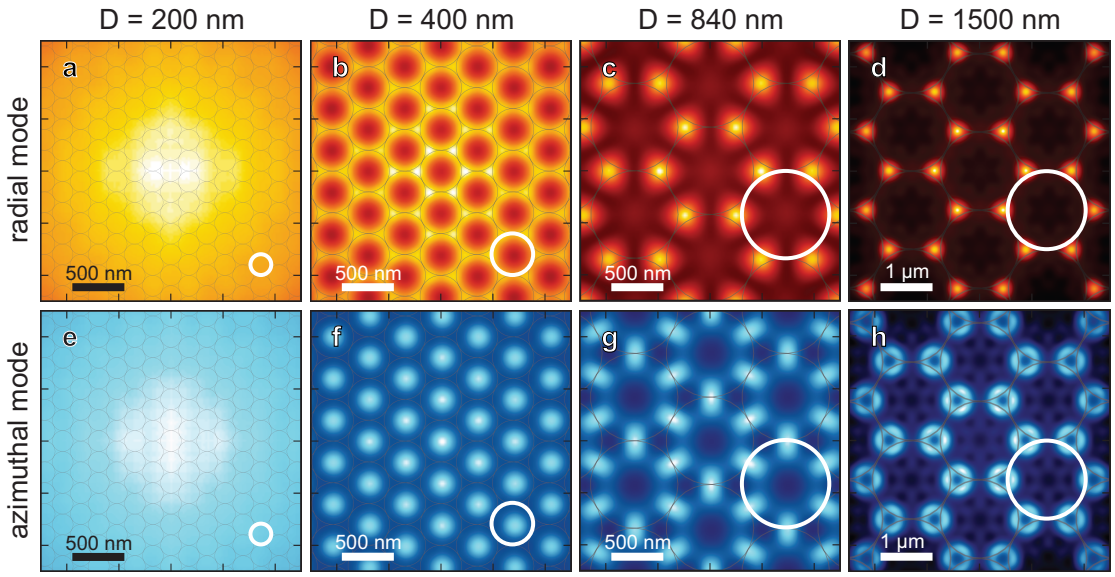

Figure 4.8: Calculated convolution of the intensity distribution in the (a)-(d) radial and (e)-(h) azimuthal focus with various Fischer patterns. The outlines of the former polystyrene sphere positions are depicted in grey and as a further guide to the eye, one bead position is drawn thicker. Note that (d) and (h) depict a larger area, analogously to the experimental scan areas. All images were computed by Josip Mihaljevic.

On the other hand, comparing the experimental images of the nano-triangles on glass (figures 4.6 and 4.7) to the theoretical patterns, I found only one matching pair: the azimuthal investigation of triangles with $h = 40\,\text{nm}$ and $L \approx 170\,\text{nm}$ (compare figure 4.7b to figure 4.8f). In all other cases, the theoretical images had no resemblance to the experimental patterns. The above stated simplifications made during these calculations have to account for this finding: the disregarding of light polarisation, the triangle height and the substrate material which ignored plasmonic processes. The deviation of the experiments from this simplified theory is hence a further proof that the measured luminescence is more than a mere light scattering on the gold. In most measurements of Fischer patterns on glass, particle plasmons were excited and could be observed by our confocal methods.

4.4 SERS on Fischer Patterns

Ultimately, I assessed the gold Fischer patterns' applicability as SERS enhancing substrates [Sti08]. To this end, I added a homogeneous layer of adenine molecules as described in chapter 4.1. As expected by the confocal studies where the triangles on glass had shown a stronger luminescence and a higher contrast, these now also proved

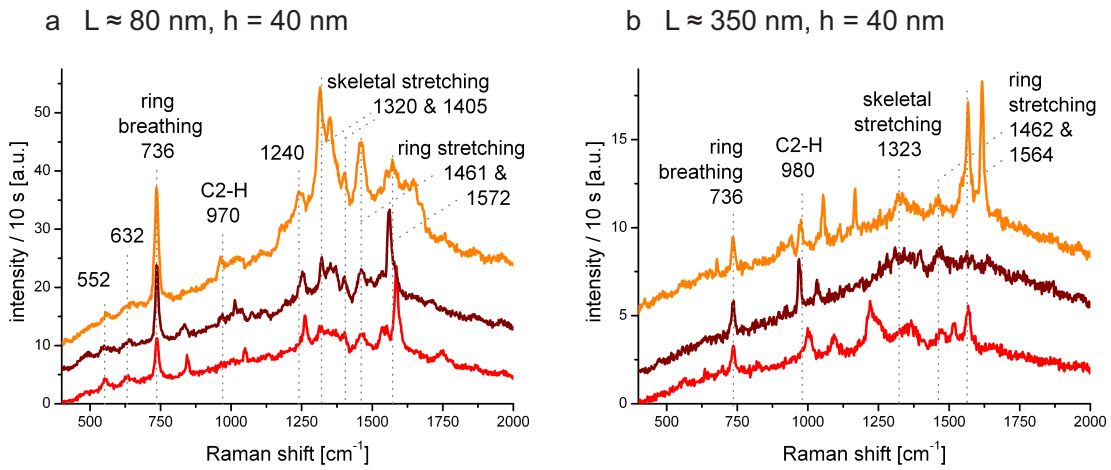

Figure 4.9: Surface-enhanced Raman spectra of an adenine (sub-)monolayer on gold Fisher patterns on glass. The nano-triangles used had an edge length of (a) $L \approx 80\,\text{nm}$ and (b) $L \approx 350\,\text{nm}$. In both cases, the gold film thickness was $h = 40\,\text{nm}$. Three spectra, offset for clarity, are shown in both cases to demonstrate the reproducibility of the measurements at different spots. All spectra were recorded in radial doughnut laser mode and with an acquisition time of 10 s.

to be better suited substrates for SERS. Especially the flat triangles ($h = 40\,\text{nm}$) on glass yielded reproducible SERS spectra in radial mode – see figure 4.9. Both on the Fischer patterns with $L \approx 80\,\text{nm}$ and with $L \approx 350\,\text{nm}$, the typical ring breathing mode of adenine was observed clearly and highly reproducible at $736\,\text{cm}^{-1}$. Further bands could be assigned according to previous SERS measurements in literature [Ott86, Gie02, Ke05, Bel06, Bar08].

Some differences can be noticed in the spectra of figures 4.9a and 4.9b. For example, the adenine ring breathing mode is stronger in figure 4.9a. Such spectral variations can be explained by the deviating particle plasmon resonance (see chapter 2.2) of the respective Fischer patterns. An optimal SERS enhancement occurs when the plasmon extinction spans over the frequencies of both the incident and the Raman scattered light [Sti08]. Hence, in the two regarded Fischer patterns, different Raman bands can be differently pronounced or can even vanish.

Three spectra are shown in each case to demonstrate the reproducibility but also the slight fluctuations in the Raman bands. The latter can be ascribed to the different adsorption positions the molecules can take e.g. on the flat top part of a triangle or at its edge. As was pointed out in chapter 2.4.1, the most efficient Raman enhancement occurs when the transition moment of a molecule is parallel to the electric near-field component [Lom08]. Hence, a diversity in adsorption positions on a short scale range can lead to fluctuations in the Raman bands. However, such a fluctuation

can only be observed if the measurement does not average over a large amount of molecules. Therefore, the measured fluctuations are a strong indicator that in the shown spectra I have detected sub-monolayer quantities of adenine.

Using the same method on the gold triangles on silicon, no Raman bands could be observed. In a final test, I investigated whether a possible reason for this could be that evaporated gold might form rougher surfaces on glass than on silicon and thereby alone cause the plasmonic enhancement. I therefore prepared an adenine monolayer on a closed gold film evaporated on glass. Here, no Raman bands were observable either, not even with an integration time of 60 s (not shown). I therefore conclude that the particle plasmon modes excited in the Fischer pattern triangles are responsible for the strong Raman enhancement observed in figure 4.9.

4.5 Conclusions

Employing higher order laser modes, I was able to excite different particle plasmon modes in gold Fischer patterns. Although with azimuthal mode it was difficult to locate the exact origin of observed high intensity spots, the more straight forward radial focus lets us pinpoint areas of intense near-field luminescence.

I investigated gold Fischer patterns on two different substrates: silicon and glass. On glass, the overall luminescence was generally much stronger than on silicon. Also, the layout of the luminescence patterns of triangles of comparable size and aspect ratio differed on silicon and on glass. These deviations have to be assigned to the great discrepancy of the dielectric constants of the two substrates.

Furthermore, Josip Mihaljevic performed a simple theoretical convolution of the higher order laser modes with each of the investigated triangle sizes. The luminescence periodicities observed on silicon largely matched this simple theory. Although I can not exclude plasmonic effects to take place, it is possible that on silicon the observed patterns were merely light scattering occurring stronger on the gold than on the silicon. On glass however, except for one matching case out of eight, the measured patterns differed fully from the computed ones. This led to the conviction that my measurements on glass had excited particle plasmons and had imaged the far-field irradiation of local near-field enhancements.

Additionally to particle plasmons in the triangles, some of the observed luminescence might also stem from a plasmonic excitement of small roughnesses at the edges of the triangles. It is known from AFM imaging that a narrow stripe of droplets occurs at the triangle borders as a by-product during evaporation [Bon07, Kol11]. This might lead to similar plasmonic luminescence as it can be observed at the edges of much larger evaporated gold squares – see figure 5.1 in the upcoming chapter 5.1.

Small gold triangles on glass also proved to be good substrates for SERS measurements: I obtained strongly enhanced Raman bands of adenine with an integration time of merely 10 second. Different triangle aspect ratios yielded slightly varying spectra. This can be explained by the selection rules for efficient Raman excitation depending on the individual particle plasmon resonance of the Fischer pattern. Moreover, I observed some fluctuations of the Raman bands which is an indication that I was able to detect a small quantity of molecules by each spectrum.

5 Investigations of DNA Strands

Raman scattering (see chapter 2.4) is a fascinating tool for the study of molecules: each compound yields a unique spectral fingerprint of Raman bands. This applies especially – yet not exclusively – to biological molecules which evolved for interaction with visible light. By means of Raman spectroscopy, different molecules are thus traceable, their concentration can be quantified and possible spectroscopic shifts occurring under certain circumstances can be monitored. However, since the Raman scattered light is of intrinsically low intensity, classical Raman spectroscopy can study only large ensembles of molecules.

Nowadays, techniques that can investigate individual molecules are in demand. In this respect, tip-enhanced Raman spectroscopy (TERS, see chapter 2.4.2) is an extremely promising method. Additionally, the implementation of TERS in our scanning near-field optical microscope (SNOM, see chapter 3.2) allows us to correlate obtained TERS signals with a measured topography. Larger molecules can thus easily be located and subsequently investigated by TERS. DNA, probably the most prominent biological molecule, is an ideal candidate for such studies.

In a preliminary sub-project, confocal surface enhanced Raman scattering (SERS, see chapter 2.4.1) of DNA was performed for a later spectroscopic reference. One aim of my further studies was to find a suitable substrate for investigating natural DNA strands by SNOM and to collect TERS spectra of these strands. In order to topographically depict the fine DNA strands, a flat – preferably atomically flat – surface was required.

The data presented here has in part been published previously [Hen10].

5.1 Confocal Investigations

5.1.1 Sample Preparation

For the electromagnetic enhancement of SERS, a plasmonically excitable substrate is essential. Here, I used the edges of evaporated gold or silver squares which exhibit a random roughness. Statistically, some of these roughnesses are expected to have matching sizes for a plasmon resonance at the wavelength of our helium-neon laser.

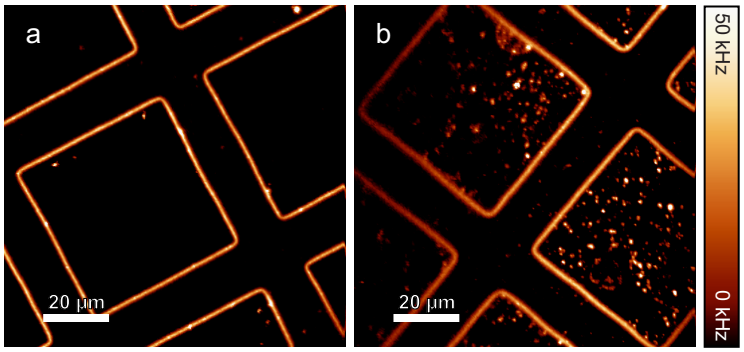

Figure 5.1: Confocal image of (a) silver edges and (b) gold edges on silicon, the latter with additional gold nano-particles. The left part of image (b) appears darker since it is out of focus due to a slight tilt of the sample.

To produce such rough edges, fine copper grids (as used in transmission electron microscopy) were employed as a mask. A single grid was carefully attached to a silicon substrate piece using tiny cuts of adhesive tape. Then, the noble metal was deposited onto the substrate in a vacuum evaporating machine (Edwards FTM7, EB3). Typically, a film thickness of 20 nm was evaporated. After removing the copper grid, I obtained a substrate covered with small metal squares with rough borders. In confocal microscopy images – see figure 5.1 – these rough edges appear as bright lines. This is due to plasmonic excitations and a subsequent metal photoluminescence emitted at red-shifted frequencies. In contrast, both the flat gold areas and the bare silicon appear dark.

A such prepared SERS substrate was then incubated with a low concentration solution of sample molecules in water[1]. The DNA base adenine (Sigma-Aldrich) and calf-thymus DNA double strands (Sigma-Aldrich) were investigated as sample molecules. After some adsorption time, the solution was removed and the sample rinsed with water in order to eliminate potentially formed multilayers.

On some samples, I additionally spin-coated gold nano-particles of 20 nm diameter on top of the molecules. The aim of this procedure was to create sandwich configurations of sample molecules between the evaporated gold surface and one or several gold nano-particles – similar to the gap-mode configuration discussed in chapter 2.2. A confocal scan of such a sample is shown in Figure 5.1b.

5.1.2 SERS of Adenine and DNA Strands

I investigated monomeric adenine and calf-thymus DNA double strands. In both cases, SERS spectra were recorded at several locations that had appeared bright in the confocal images. The spectra shown in figure 5.2 were obtained on gold edges as well as at locations of gold nano-particles.

[1] Over the whole course of this work, all water employed for the preparation of samples was either deionised and then triple distilled water or Millipore water.

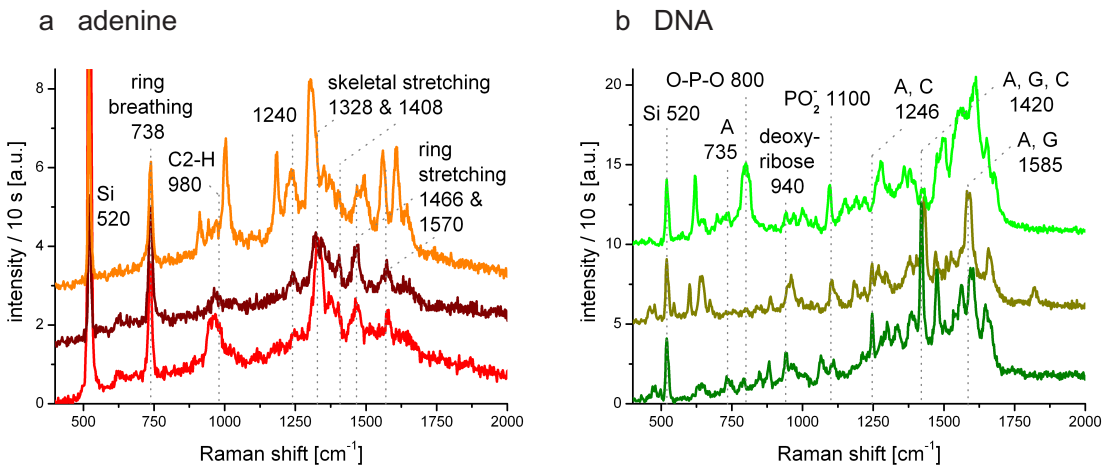

Figure 5.2: Surface-enhanced Raman spectra (a) of adenine and (b) of calf-thymus DNA double strands. The substrates were rough gold edges on silicon with additionally spin-coated gold nano-particles. In both cases, three offset spectra show the SERS reproducibility. Each was collected with an integration time of 10 s. In (b), the letters A and C designate the DNA bases adenine and cytosine respectively.

In all spectra, the well-known silicon Raman line appeared at 520 cm^{-1}. The spectra shown in figure 5.2a were mainly recorded at the rough gold edges. Here, the silicon peak emerged particularly strong. The spectra depicted in figure 5.2b on the other hand were collected at 'hot spots' created by gold nano-spheres on the closed gold surface. In this case, the silicon signal is weaker due to the decaying light intensity as passing the gold [Loe72].

As in the case of Fischer patterns acting as SERS substrates (chapter 4.4), the adenine ring breathing mode was visible at around 735 cm^{-1} (see figure 5.2a). This band was also visible when investigating DNA strands (figure 5.2b). Among the four DNA bases, adenine has the largest cross-section. Therefore, its vibration modes were observed more often in the DNA SERS spectra compared to those of the other bases. To exemplify, I assigned some additional Raman peaks [Ott86, Gie02, Ke05, Bel06, Bar08].

5.2 Near-Field Investigations

5.2.1 Sample Preparation and Topographical Characterisation

I tested three different substrates on which I immobilised DNA double strands (calf-thymus DNA, Sigma-Aldrich) for SNOM topographical measurements and subse-

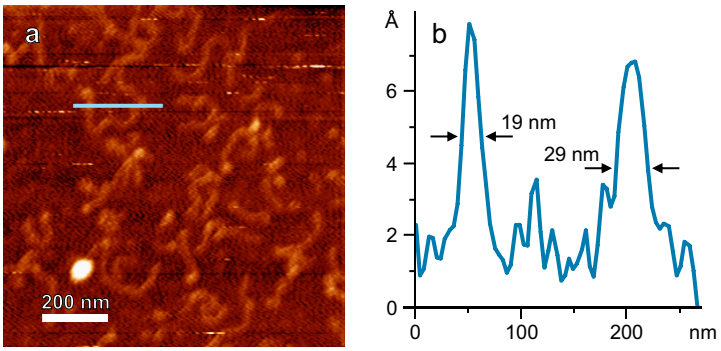

Figure 5.3: Shear-force image of calf-thymus DNA strands on mica and an associated line-section. On the latter, one smoothing step had been conducted in WSxM [Hor07].

quent TERS investigations. The first substrate was mica; the second a commercial gold (111) monocrystal[2]. The third substrate was a commercial gold (111) surface (Arrandee).

DNA Strands on Mica

Mica is frequently employed as a substrate for DNA imaging by AFM or scanning probe microscopy (SPM) in general [Zen92, Pas03, Bai08]. Thin mica layers are almost transparent, which is an advantage in SNOM setups that illuminate the sample from below [Bai08]. This is, however, a feature we do not have to rely on in our top-illuminating setup.

Since both the backbone of DNA and the surface of mica are slightly negatively charged, it is necessary to mediate the contact by positive ions [Han96, Pas03]. For the sample preparation I closely followed the protocol by Pastré et al. [Pas03]. I used a freshly cleaved piece of mica (Plano) and pre-treated it with a 20 µl droplet of 10 mM $NiCl_2$. After 1 min, the mica was thoroughly rinsed with water and dried.

Calf-thymus DNA was prepared in a buffer solution. I diluted to 0.5 µg/ml final concentration of DNA in 10 mM tris, 10 mM NaCl and 2 mM $MgCl_2$ aqueous solution. In order to fracture the long calf-thymus DNA strands – naturally consisting of millions of base pairs – into shorter pieces, I put the solution in a weak ultrasound bath for 6 min. I then placed a 20 µl droplet of this solution on the pre-treated mica piece. The substrate was incubated with the DNA solution for 3 min before it was washed and again dried.

Topographical shear-force measurements of the surface were performed in our setup, see figure 5.3. The strands appear to be scarcely 1 nm high, even though DNA double strands have a diameter of approximately 2 nm [Atk10]. This deviation is known for imaging DNA in SPM: the softer DNA strands appear flatter on the harder substrate [Zen92]. The forces acting between tip and sample both in AFM and in shear-force microscopy differ according to the local sample material [Gro10].

[2](111) stands for the (hkl) Miller indices of the crystalline surface.

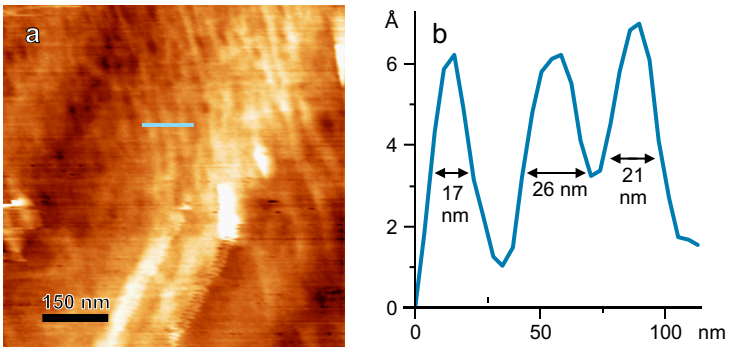

Figure 5.4: Shear-force image of calf-thymus DNA strands on a gold (111) crystal. The topographical image as shown here was processed by a parabolic flattening and the line-section by one smoothing step.

DNA Strands on a Gold Monocrystal

In a second experiment, the substrate was a commercial gold (111) monocrystal with a diameter of 5 mm. For cleaning in between experiments, it was immersed into freshly prepared piranha solution (sulfuric acid H_2SO_4 and hydrogen peroxide H_2O_2) over night. After rinsing the crystal thoroughly with water, it was flame-annealed for at least 5 min. I took care never to heat the crystal up to red glowing. It was then left to cool in air.

A solution of 1600 µg/ml calf-thymus DNA in water was prepared and weakly sonicated for 5 s to 10 s. The gold monocrystal was immersed into this solution for 2 h, then rinsed three times in abundant water.

Again, I performed a topographical characterisation in our setup, see figure 5.4. Here, too, the DNA double strands appear to be less than 1 nm in height.

DNA Strands on Arrandee Gold Substrates

Commercial gold substrates (Arrandee) were cut to square pieces of 5 mm edge length with a wafer cutter. These substrates were freshly flame-annealed in consecutive heating cycles with approximately 30 s pauses in between. The total annealing time was at least 5 min, after which the sample was left to cool in air. By this treatment, atomically flat (111) crystalline areas formed on the surface.

A solution of 80 µg/ml calf-thymus DNA was prepared in water and weakly sonicated for 60 s in order to untangle the DNA strands. A small Arrandee substrate was then fully immersed in a large volume of this DNA solution. For approximately 75 min, the DNA was left to adsorb on the surface. Afterwards, the sample was rinsed three times with plenty of water.

A topographical shear-force measurement of a thus prepared sample is shown in figure 5.5. The DNA strands have the same apparent height as previously on mica and on the gold monocrystal.

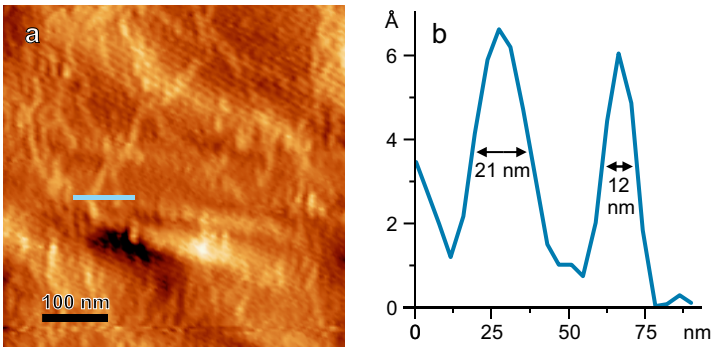

Figure 5.5: Shear-force image of calf-thymus DNA strands on an annealed Arrandee gold (111) surface. A parabolic flattening was performed on this image and one smoothing step on the line-section.

5.2.2 TERS of DNA Strands

With mica as a substrate, my attempts to observe TERS failed: no Raman bands could be detected in the noise of the luminescence which originated from the employed gold tip. However, mica as a substrate cannot yield the multiplied enhancement occurring between a tip and its plasmonic mirror image inside a metal substrate as discussed in chapter 2.3.

As aimed for, I achieved such a gap mode 'hot spot' both with the gold monocrystal and with the Arrandee substrates. By stepwise increasing the phase-shift of the tuning fork feedback, the distance between tip and sample was decreased until strong Raman bands appeared in the spectrum. One such approach of tip and sample is shown in figure 5.6 for each of the two gold substrates.

As in the above discussed SERS spectra (figure 5.2), the detected Raman peaks could be assigned to vibration modes of molecular constituents of DNA according to previous SERS and TERS publications [Ott86, Gie02, Ke05, Bel06, Dom07, Bar08]. Overall, less Raman bands were observed in TERS than in SERS. Similar to my previous SERS findings on Fischer patterns (chapter 4.4), this can be explained by the selection rules of efficient Raman excitation as mentioned in chapter 2.4.1. Raman modes parallel to the electric field are excited most efficiently [Lom08]. In the case of rough SERS surfaces, the locally enhanced electric fields have various orientations. Likewise, molecules adsorbed on such a surface have all kinds of alignment. This allows for many Raman modes to be excited and hence observed in SERS.

In the case of the atomically flat gold monocrystal on the other hand, the electric field is perpendicular to the surface. Furthermore, all of the molecules are likely to have very similar orientations as they bind to the flat surface. Although TERS allows for a more controlled Raman excitement and signal collection, this homogeneity allows for the effective enhancement of only a part of the bands that were observable in my SERS measurements.

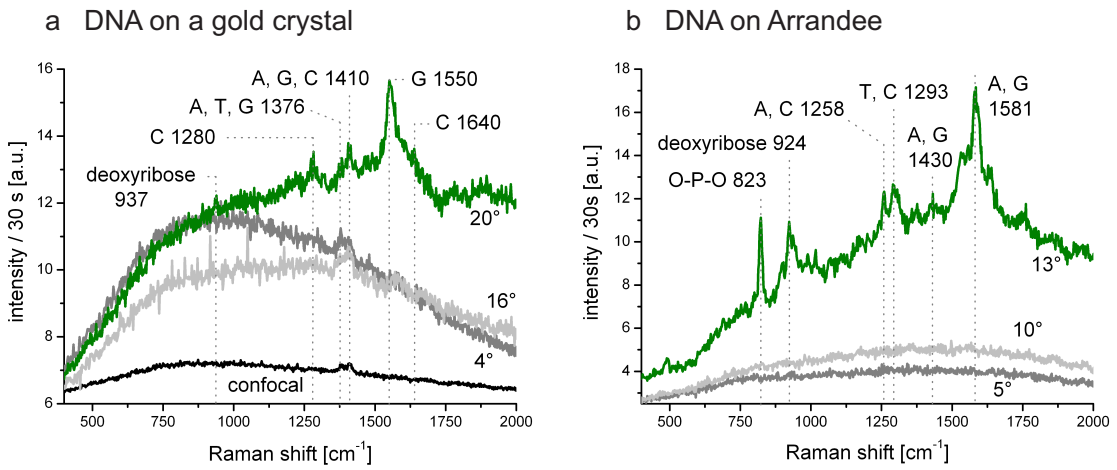

Figure 5.6: TERS spectra of calf-thymus DNA (a) on a gold (111) monocrystal and (b) on a gold (111) Arrandee surface. In each case, several consecutive spectra show a stepwise approach of the tip to the sample, measured as an increasing phase shift of the tuning fork's frequency in degrees (see chapter 3.2.4), as indicated next to each spectrum. All spectra employing the tip were recorded with an integration time of 30 s. The confocal spectrum in (a) was collected over a period of 2 min and later normalised to a 30 s integration. In assigning the Raman bands, A, T, G and C designate the DNA bases adenine, thymine, guanine and cytosine respectively.

TERS on the Gold Monocrystal

On the gold monocrystal, I observed first a red-shift of the luminescence maximum – see the light grey 16° spectrum in figure 5.6a. Such a red-shift had been detected in a previous work [Zha10] and I noted it in several more acquisitions of TERS spectra during the course of this work. As described by the Mie theory (see chapter 2.2), increasing the size of a nano-particle shifts its luminescence to longer wavelengths. Thus, the observed red-shift is an indication for a coupling of the tip to the gold substrate: they start to act as one plasmonic unit. It remains unclear at this point, why the intensity at the spectral maximum is less in the 16° spectrum than in the 4° spectrum. My other TERS approaches usually showed a continuous increase of the PL intensity.

At a 20° phase-shift, the total spectral intensity increased drastically. Additionally, typical Raman bands of DNA became visible. A confocal far field spectrum collected at the same location is shown for comparison in the same figure 5.6a.

The TERS enhancement factor was calculated according to equation 3.1 (page 29): $F_{enh} = I_{nearf} \cdot A_{farf} / I_{farf} \cdot A_{nearf}$. I assessed the enhancement of this data set based on the Raman band at 1550 cm^{-1}. In the tip-enhanced spectrum, the peak rises 4.52 arbitrary units (a.u.) above the gold luminescence. Since this band did not appear

in the corresponding confocal spectrum, it had to be smaller than the noise level of 0.078 a.u. in this region.

Corresponding to the known focal diameter of 260 nm (see figure 3.3b on page 24), the area excited in confocal far field mode is $\pi \cdot (130\,\mathrm{nm})^2 = 5.31 \cdot 10^{-14}\,\mathrm{m}^2$. With TERS, the area of excitation is given by the tip apex diameter. In the corresponding topographical image (figure 5.4), I observed the DNA strands to be 17 nm in diameter. This measure has to be regarded as a convolution of the tip apex and the much thinner DNA strands. I could thus conclude that the apex diameter of the employed tip was 17 nm. Hence, the near-field area was $2.27 \cdot 10^{-16}\,\mathrm{m}^2$.

With these numbers, I calculated the enhancement factor to be at least $F_{enh} \gtrsim 1.4 \cdot 10^4$. Furthermore, given the topographical convolution of 17 nm, I conclude that merely a fraction of one single DNA strand was excited by TERS in the enhanced 20° spectrum shown in figure 5.6a.

TERS on Arrandee

With the Arrandee crystalline gold substrate, I recorded a similar TERS approach – see figure 5.6b. Here, the Raman bands appeared already at a phase-shift of 13° and hence much earlier than on the gold crystal. However, not enough of such strongly enhanced TERS approaches could be recorded in order to evaluate if this deviation is due to the different substrates or merely to the variances of the individual tips used in the two measurements of figure 5.6.

I computed the TERS enhancement factor analogously to the TERS approach on the gold monocrystal. Here, I considered the 5.99 a.u. high Raman band at $1581\,\mathrm{cm}^{-1}$. In this data set, no confocal spectrum was recorded. However, the spectrum at a phase-shift of 4° exhibited no Raman bands and thus served as the non-enhanced far-field reference. Again, the intensity of the $1581\,\mathrm{cm}^{-1}$ band has to be below the 0.33 a.u. noise level in this spectrum.

In a topographical image measured with the same tip (not shown), the smallest features had a diameter of 16 nm. Thus, the near-field area can be estimated to be $2.01 \cdot 10^{-16}\,\mathrm{m}^2$. The lower limit for the enhancement factor can then be calculated to $F_{enh} \gtrsim 4.8 \cdot 10^3$.

5.3 Conclusions

I collected SERS spectra of both adenine and natural DNA strands on rough gold edges with additional gold nano-particles. I observed reproducible yet slightly fluctuating SERS bands. The latter is an indication that I was able to detect very low numbers of molecules by Raman spectroscopy.

In performing TERS spectroscopy of natural DNA strands, I found it easier to achieve a Raman enhancement on gold than on mica – although Bailo and Deckert had previously been able to perform TERS of poly-cytosine RNA on mica [Bai08]. Still, due to the mirror charges which can only occur in metals, stronger TERS signals can be expected on gold. Thus, I suggest flat, i.e. crystalline gold surfaces as the substrates of choice for further suchlike investigations.

With TERS on a gold monocrystal, the enhancement factor was found to be $F_{enh} \gtrsim 1.4 \cdot 10^4$; on an Arrandee gold crystalline surface, I measured a factor of $F_{enh} \gtrsim 4.8 \cdot 10^3$. From the measured lateral resolution I concluded to have collected TERS spectra of only a fraction of one DNA double strand in both cases.

Both the spectral SERS and the TERS bands could be assigned to vibration modes found previously by other researchers [Ott86, Gie02, Ke05, Bel06, Dom07, Bar08]. I observed several spectral correspondences between the SERS and the TERS peaks of DNA, although overall more bands were observed by SERS. This can be explained by the large variety of both the enhanced electric field vectors on the rough SERS substrate and of the molecular orientations in this case. In the more uniform alignment of TERS, not all of the Raman bands can be efficiently excited and thus measured.

6 Near-Field Investigations of Amyloid Fibrils

Amyloid fibrils are misfolded yet highly ordered aggregates of proteins [Dob03]. Under certain – mostly non-physiological – conditions, a large variety of proteins can adopt this configuration. The formation of amyloid fibrils within the human body is believed to be responsible for several medical conditions including Alzheimer's and Parkinson's disease. However, even several functional occurrences of amyloid fibrils have been found, e.g. in bacteria, yeast and fungi [Ham08].

Although amyloid fibrils have previously been investigated by SERS [Ort07, Bei07, Cho08], only one preliminary TERS report is known to me [DG10]. Since the amyloid strands are several nanometres in diameter and can easily be immobilised on flat gold surfaces [Bül10b], they seemed to be optimal specimen for our custom-built SNOM. Being roughly 10 times as thick as DNA strands, we expected their topographical imaging to be even easier than that of DNA. The further aim was to subsequently collect TERS spectra on individual amyloid strands.

I investigated two kinds of amyloid fibrils: insulin amyloid and hen egg white lysozyme (HEWL) amyloid. The measurements presented here were a collaboration with Alexander Büll [Bül11] from the research group of Professor Mark Welland at the University of Cambridge, UK. The group has previously worked extensively with amyloid fibrils [Whi09, Bül10a, Bül10b].

6.1 Sample Preparation

All samples were prepared by Alexander Büll. As a first step, he created ultra-flat gold substrates by so-called template-stripping [Wag95]: gold was evaporated onto freshly cleaved mica, the gold side was then glued to a piece of silicon before finally removing the mica. The conductivity of the thus obtained gold surface was checked With a multimeter to confirm that all mica layers had been stripped.

Protein gels were created by dissolving the proteins to a concentration of approximately 1 mM to 2 mM (5 to 10 g/l for insulin and 15 to 30 g/l for lysozyme) in

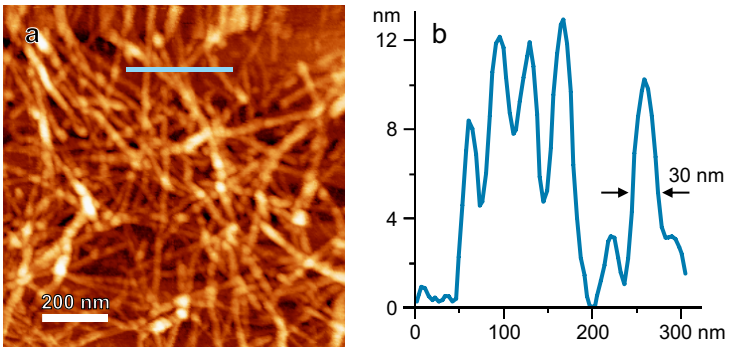

Figure 6.1: Topography of insulin amyloid fibrils on a template-stripped gold surface. The image was obtained by scanning the tip over the sample using shear-force feedback. One smoothing step was conducted in WSxM on the depicted line-section.

hydrochloric acid solution (HCl) at pH 2 and heating the solution to 60 °C. By this treatment, fibril formation is induced, slowly turning the fluids into gels. In order to accelerate the amyloidogenic reaction (which would otherwise take approximately 2 weeks), NaCl was added up to a concentration of 20 mM and the solution was agitated with a magnetic stirrer.

In the final sample preparation, these gels were diluted by a factor of approximately 1 : 100 in hydrochloric acid of pH 2 and mixed thoroughly. The gold substrate was incubated with a small volume of this amyloid fibril solution for 30 min to 1 h. Afterwards, the sample was rinsed carefully with hydrochloric acid solution, pH 2 and left to dry.

6.2 Topographical Investigations

To characterise the amyloid fibril samples, I investigated their topography by scanning probe microscopy in our setup (see chapter 3.2.1). Since I expected the surface to be packed closely and homogeneously with fibrils, I employed the tip-scanning mode as described in chapter 3.3.

Tip-Scanning Shear-Force Mode

I imaged insulin amyloid fibrils by scanning the tip over the stationary sample. As a feedback mechanism, I employed the earlier described shear-force of a quartz tuning fork.

Figure 6.1 shows a thus obtained topographical recording. One can clearly see a large amount of fibrils being densely packed and often overlapping on the surface. Most fibrils were found to be in the order of 10 nm in height. However, some had approximately half this height. The latter can be recognized as so-called protofilaments, a preliminary state of amyloid formation [Dob03]. Often, two such protofilaments wrap around each other to form an amyloid fibril.

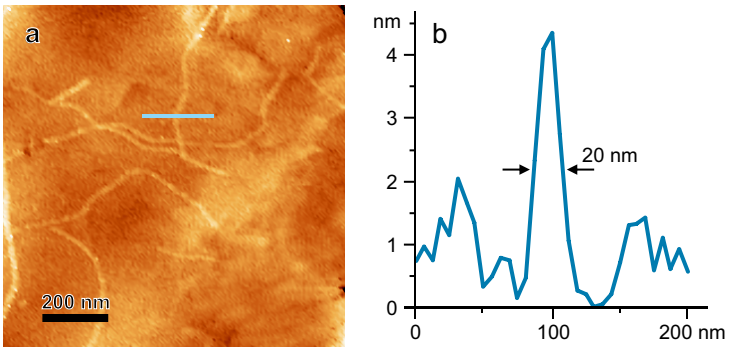

Figure 6.2: Low concentrated HEWL amyloid fibrils on gold. For this recording, the tip was scanned over the sample surface in STM feedback. The topographical image was parabolically flattened and the line-section slightly smoothed.

Tip-Scanning STM Mode

As mentioned in chapter 3.2.1, the possibility to use a tunnelling current as a topographical feedback variable was implemented during a later stage of this work. I used this STM mode to picture hen egg white lysozyme fibrils; see figure 6.2.

Few individual amyloid strands were topographically depicted and found to be approximately 5 nm high. Comparing them to the previous measurement of insulin amyloid, I therefore assume these HEW fibrils to be in the proto-filament state.

6.3 TERS of Amyloid Fibrils

I collected TERS spectra of insulin amyloid fibrils on a template-stripped gold surface – see figure 6.3. As in previous TERS approaches (see chapter 5.2.2), I observed first a red-shift of the luminescence maximum. Upon further decreasing the tip-sample gap size, three strong Raman bands became visible.

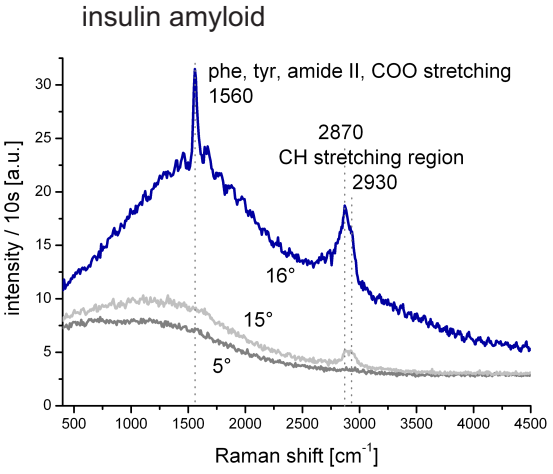

Figure 6.3: TERS approach spectra of insulin amyloid fibrils on a template-stripped gold surface. The phase shift – given in degrees next to each spectrum – is a measure for the tip-sample distance (see chapter 3.2.4). Each spectrum was collected with an integration time of 10 s. The amino acids phenylalanine and tyrosine are abbreviated by phe and tyr, while amide II denotes the NH bending in the amide group.

As previously, I attributed the red-shift to a plasmonic coupling of the tip to the gold substrate. The measured Raman lines were assigned bona fide according to literature values. As indicated in figure 6.3, the strong peak at $1560\,\mathrm{cm}^{-1}$ lies in the spectral region of several known Raman bands [Cho08]. Deckert-Gaudig et al. also measured their most dominant TERS band in this region [DG10]. The two bands just below $3000\,\mathrm{cm}^{-1}$ could be associated to the CH stretching [Ort07].

I determined the TERS enhancement factor of this data set by evaluating the band at $1560\,\mathrm{cm}^{-1}$. As previously with the DNA measurements, I calculated it via $F_{enh} = I_{nearf} \cdot A_{farf} / I_{farf} \cdot A_{nearf}$ (equation 3.1). The peak at $1560\,\mathrm{cm}^{-1}$ is 910 arbitrary units bright above the gold luminescence. I used the non-enhanced spectrum collected at a phase shift of 5° as a far-field reference. In the region of this Raman band, its noise is approximately 37 a.u. high.

The smallest topographical features observed on this measurement day and with this tip had an FWHM of 19 nm (not shown). Hence, I deduced a tip apex near-field area of $2.84 \cdot 10^{-16}\,\mathrm{m}^2$, compared to a confocal area of $5.31 \cdot 10^{-14}\,\mathrm{m}^2$.

Multiplying the enhancement found by comparing on the one hand the intensities and on the other hand the excited areas, I calculate a total enhancement factor of $F_{enh} \gtrsim 4.6 \cdot 10^3$. Again, this is merely a lower limit for the enhancement, since I could only use the noise as an upper boundary for the non-observed Raman band in the far-field case.

6.4 Conclusions

I investigated insulin and hen egg white lysozyme (HEWL) in amyloidogenic form. The amyloid fibrils had been immobilised on template-stripped gold surfaces. Using our setup, I obtained clear topographical images of both of these samples. Insulin amyloid was measured using the shear-force feedback mechanism, HEWL amyloid employing an STM feedback.

On the insulin amyloid, I successfully conducted a TERS approach and measured enhanced Raman bands which could be assigned to literature values. The enhancement factor was subsequently calculated to be $F_{enh} \gtrsim 4.6 \cdot 10^3$.

7 Concluding Remarks and Outlook

Scanning near-field optical microscopy (SNOM) and tip-enhanced Raman scattering (TERS) as general methods have passed the proof-of-principle stage [Har08, Dec09, Dom10]. However, state-of-the-art SNOM and TERS are still done on custom-built setups; therefore, each design has to go through this phase individually. In this work, I have affirmed the possibilities of our SNOM setup to investigate biological molecules. Valuable results for adenine, DNA and amyloid fibrils have been presented.

Our setup operates at room temperature and in air. It can investigate non-transparent samples. Its special features include a parabolic mirror as the element both for focusing the laser light and for collecting the scattered signal from the sample. Its high collection angle of almost 180° stretching above the sample allows to collect as much of the scattered signal as possible. We employ higher order laser modes to achieve a highly confined focus for confocal optical scans and to be able to switch between a focal polarisation in sample plane (x, y) or perpendicular to it (z). More importantly even, the strong z-polarisation is used to efficiently excite a gold tip. This tip thus acts as a topographical probe and a plasmonically excited optical antenna in one. In its second function, it allows us to collect TERS spectra.

Our parabolic mirror based scanning near-field optical microscope proved to be a good and flexible setup for various approaches to biological molecules. In this work, I investigated three sets of samples: gold Fischer patterns, DNA double strands and amyloid fibrils.

Plasmonics of Gold Fischer Patterns

As a means to obtain a controllable and thus systematically improvable substrate for SERS measurements, I investigated gold Fischer patterns: regular arrays of nanotriangles. I performed confocal scans in both radial and azimuthal laser mode on triangles of different height and edge length on two different materials, namely silicon and glass.

I was able to map the far-field radiation of near-field 'hot spots' of such Fischer patterns. The luminescence patterns I recorded in this way differed greatly on silicon and glass. In general, I obtained stronger luminescence and a higher contrast

on glass. The patterns also varied with the height and the edge length of the triangles.

I compared my measurements to a simple convolution calculation of the respective focal intensity and the respective triangle sizes. This allowed for the distinction between the samples on which particle plasmons were most probably excited and those samples where the assumption of a superficial light scattering might suffice to explain the observed patterns.

SERS spectra of the DNA base adenine were obtained on the two smallest investigated gold triangles on glass.

As an outlook for the future, our systematic approach of investigating different triangle aspect ratios should undoubtedly be extended. For example, triangles created by beads of a diameter $D = 1500\,\mathrm{nm}$ were not yet investigated on a glass substrate. The height h of the triangles could be varied to a greater extent. Additional data should be collected between and beyond the two main height values $40/50\,\mathrm{nm}$ and at the other extreme $150/200\,\mathrm{nm}$ which were measured so far. Since the smallest investigated triangles on glass yielded promising results as SERS substrates, they should be investigated more thoroughly and with small alteration steps of the aspect ratios.

By taking out the mode-converter entirely, the gold Fischer patterns could be investigated with a Gaussian laser mode. In the focus centre, this mode has a linear polarisation in the sample plane. Although the size of this focus is slightly larger than that of our radial mode, is might enable a better understanding of in-plane plasmons than the azimuthal doughnut mode. Additionally, a better comparison to the findings of Boneberg et al. [Bon07] would be possible this way.

Further insight into the plasmonic response could be obtained by carefully evaluating photoluminescence (PL) spectra of Fischer patterns without any molecules. Such spectra should be taken in both radial and azimuthal mode systematically on several points of the luminescence patterns. Even better, a spectral mapping as has been implemented to our setup recently could be performed. In spectral mapping, the XPMPro software waits for WinSpec to collect a spectrum at each pixel location defined in the XPMPro settings. This data can then be put together to intensity images of individual spectral regions, thus mapping luminescence shifts [Wan10].

In the end, such a thorough investigation would guide us to the best possible Fischer pattern yielding the highest achievable plasmonic enhancement for SERS investigations. Establishing Fisher patterns as standard SERS substrates would enable an easy and reliable comparison of SERS results of different research groups worldwide. Moreover, the strong 'hot spots' of Fischer patterns might allow for single molecule SERS to become achievable reproducibly.

Investigations of DNA Strands

I investigated the DNA base adenine and natural calf-thymus DNA double strands by SERS and detected very low concentrations of the molecules. I topographically imaged individual DNA double strands immobilized on crystalline gold surfaces and collected TERS spectra. The Raman enhancement factor was at least in the order of 10^3 or 10^4. Many of the Raman bands found by SERS and TERS matched literature values.

As for future investigations, the template-stripped gold substrates as prepared by Alexander Büll should also be tested as a substrate for SNOM and TERS measurement of DNA strands.

The next step should be to achieve a higher reproducibility of TERS measurements. Thereto, a higher precision and stability should be aimed at in order to reliably be able to perform TERS approaches at exact sites of choice in the topographical image.

As soon as TERS along DNA strands becomes a routine measurement on our setup, we could even monitor the site-specific interaction with other molecules such as proteins or drugs. TERS spectra at the exact binding site of a single protein to an individual DNA strand could lead to insights which present-day ensemble measurements cannot provide.

The necessary precision and stability might very well be achieved soon with the STM feedback option that is now implemented in our system.

Near-Field Investigations of Amyloid Fibrils

Investigating amyloid fibrils on a flat gold surface, I could image insulin amyloid and hen egg white lysozyme amyloid topographically. I obtained TERS spectra of insulin amyloid with a Raman enhancement factor in the order of again 10^3 minimum.

The hereby started work on amyloid should be continued and expanded. As next steps, TERS spectra of protein monomers on a gold substrate could be collected and thus compared to our TERS measurements of amyloid of the same protein. It would also be rewarding to study individual amyloid strands in different states of amyloid formation. Such measurements would hopefully yield spectroscopic insight into the misfolding process of proteins.

We have not yet investigated amyloid fibrils which are explicitly associated with certain medical conditions. Beta amyloid for example forms the amyloid plaques found in Alzheimer's disease patients; alpha-synuclein amyloid is associated with Parkinson's disease. Once the fundamental SNOM and TERS principle is fully established on amyloid fibrils in general, measurements on such potentially toxic fibrils and proto-filaments could be the next step to undertake.

Zusammenfassung

Die aperturlose optische Rasternahfeldmikroskopie (SNOM) ist eine Entwicklung der letzten zwei Jahrzehnte. Sie ist eine Kombination aus Rastersondenmikroskopie, die ein topografisches Höhenprofil der Oberfläche liefert, und optischer Methoden. Dafür wird die Rasterspitze gleichzeitig als optische Antenne eingesetzt. Das Nahfeld am Spitzenende liefert dann simultan ein Lumineszenz-Bild. Dessen laterale Auflösung ist unabhängig von der Lichtwellenlänge und nur durch die Größe des Spitzenendes bestimmt; so kann die klassische optische Auflösungsgrenze umgangen werden.

In unserem Fall dient eine feine Goldspitze als Rastersonde und optische Antenne in einem. Sie wird in den Fokus eines Parabolspiegels gebracht, der wiederum von einem radialen Lasermodus höherer Ordnung bestrahlt wird. Das sorgt im Fokus für eine starke Lichtpolarisation entlang der Spitzenachse. Dadurch werden die Elektronen im Leitungsband des Goldes zu Schwingungen angeregt: im resonanten Fall spricht man von Plasmonen-Resonanzen. Diese Plasmonen wiederum sorgen für ein intensives und stark lokalisiertes elektromagnetisches Nahfeld in dem feinen Spalt zwischen Spitzenende und Probe.

Dank dieses verstärkten Nahfeldes können wir zudem spitzenverstärkte Raman-Spektren (TERS) aufnehmen. Die inelastische Raman-Streuung an Molekülen erlaubt dabei eine spezifische Zuordnung der angeregten Molekülschwingungen und damit der vorliegenden Moleküle. Unser SNOM-Mikroskop arbeitet bei möglichst natürlichen Bedingungen, d.h. an Luft und bei Raumtemperatur. Durch die Beleuchtung von oben können auch undurchsichtige Proben vermessen werden.

In dieser Arbeit habe ich die Probenuntersuchung mittels SNOM in unserem Labor auf biologische Moleküle ausgeweitet.

Zunächst untersuchten ich in konfokalem Modus, ohne den Einsatz einer Spitze, regelmäßige Anordnungen von Gold-Nanodreiecken. Diese sogenannten Fischer-Muster sollten später als Substrate für oberflächenverstärkte Raman-Spektren (SERS) dienen. Zu diesem Zweck prüfte ich systematisch ihre plasmonischen Eigenschaften. Die Arbeit an diesen Proben war eine Zusammenarbeit mit der Arbeitsgruppe von Professor Leiderer, Universität Konstanz; Andreas Kolloch stellte die hier untersuchten Fischer-Muster her. Ich studierte unterschiedliche Fischer-Muster eingehend mit den beiden Laser-Modi, die uns in unserem Messaufbau zur Verfügung stehen: einem

radialen und einem azimutalen Modus. Ersterer sorgt für eine starke vertikale, zweiterer für eine ausschließlich horizontale Lichtpolarisation im Fokus. So konnte ich gezielt unterschiedliche Plasmonen-Modi in den Dreiecks-Anordnungen anregen. Ich untersuchte und verglich auf diese Art Fischer-Muster aus Dreiecken unterschiedlicher Kantenlänge und Höhe auf zwei verschiedenen Materialien, nämlich Silizium und Glas. Dies sollte mich zu einem idealen Substrat für SERS-Messungen führen. Auf den kleinsten der untersuchten Dreiecke auf Glas erhielt ich schließlich stark verstärkte Raman-Spektren von wenigen Molekülen der DNA-Base Adenin. Die dabei gemessenen Spektrallinien konnte ich Literaturwerten zuordnen.

Die Desoxyribonukleinsäure (DNA) ist wohl das bekannteste Biomolekül. So war ein naheliegendes Ziel dieser Arbeit, einzelne DNA Stränge auf einem flachen Goldsubstrat zu fixieren und per SNOM zu untersuchen. Die Plasmonen, die in der Goldspitze angeregt werden, sorgen für Spiegelladungen in der Goldoberfläche. Dadurch wiederum wird in der schmalen Lücke zwischen Spitze und Probe ein besonders intensives Nahfeld erzeugt. Sowohl auf einem Gold-Einkristall als auch auf kommerziellen kristallinen Gold-Oberflächen gelang die topografische Abbildung und die Aufnahme von TERS Spektren. Der TERS Verstärkungsfaktor lag dabei in einer Größenordnung von mindestens 10^3 bis 10^4. Als Referenz nahm ich außerdem SERS-Spektren an rauen Kanten aufgedampften Goldes und zusätzlichen Gold-Nanopartikeln auf. Sowohl die SERS- als auch die TERS-Spektrallinien von DNA konnte ich erfolgreich mit Werten aus bisherigen Veröffentlichungen abgleichen.

Als drittes Teil-Projekt dieser Arbeit untersuchten wir – wieder auf glatten Gold-Oberflächen – sogenannte Amyloid-Fibrillen. Diese abnormen Anreicherungen von Proteinen zu langen geordneten Strängen sind Indikatoren für etliche Krankheiten, unter anderem findet man sie bei Alzheimer- und Parkinson-Patienten. Die von uns vermessenen Amyloid-Proben wurden von Alexander Büll hergestellt, der in der Arbeitsgruppe von Professor Mark Welland, Universität Cambridge, Vereinigtes Königreich, arbeitet. Wie zuvor bei der DNA erhielten wir sowohl topografische Aufnahmen als auch spitzenverstärkte Spektren. Wieder lag der gemessene Verstärkungsfaktor der TERS-Spektren bei mindestens 10^3. Auch bei den Amyloid Fibrillen gelang eine Zuordnung der beobachteten Raman-Banden zu Werten aus der Literatur.

Diese Ergebnisse belegen, dass unser selbsterstellter SNOM-Messaufbau sehr gut für die Untersuchung von Biomolekülen geeignet ist. Die im Laufe dieser Doktorarbeit gewonnenen Erkenntnisse zeigen das Potential dieser Methode und bereiten die Basis für weitergehende SNOM- und TERS-Messungen an biologischen Molekülen.

Bibliography

[Abb73] E. Abbe, *Beiträge zur Theorie des Mikroskops und der mikroskopischen Wahrnehmung*, Archiv für Mikroskopische Anatomie **9**, p. 413 (1873), dx.doi.org/10.1007/BF02956173. 8

[Alb77] M. G. Albrecht and J. A. Creighton, *Anomalously Intense Raman Spectra of Pyridine at a Silver Electrode*, Journal of the American Chemical Society **99**(15), p. 5215 (1977), dx.doi.org/10.1021/ja00457a071. 15

[Ank08] J. N. Anker, W. P. Hall, O. Lyandres, N. C. Shah, J. Zhao and R. P. Van Duyne, *Biosensing with Plasmonic Nanosensors*, Nature Materials **7**(6), p. 442 (2008), dx.doi.org/10.1038/nmat2162. 16

[Atk10] P. Atkins and J. de Paula, *Atkins' Physical Chemistry*, Oxford University Press: Oxford, UK, 9th edition (2010). 52

[Bai08] E. Bailo and V. Deckert, *Tip-Enhanced Raman Spectroscopy of Single RNA Strands: Towards a Novel Direct-Sequencing Method*, Angewandte Chemie International Edition **47**(9), p. 1658 (2008), dx.doi.org/10.1002/anie.200704054. 3, 4, 13, 18, 19, 20, 52, 57

[Bar08] A. Barhoumi, D. Zhang, F. Tam and N. J. Halas, *Surface-Enhanced Raman Spectroscopy of DNA*, Journal of the American Chemical Society **130**(16), p. 5523 (2008), dx.doi.org/10.1021/ja800023j. 45, 51, 54, 57

[Bei07] H. Beier, C. Cowan, I.-H. Chou, J. Pallikal, J. Henry, M. Benford, J. Jackson, T. Good and G. Coté, *Application of Surface-Enhanced Raman Spectroscopy for Detection of Beta Amyloid Using Nanoshells*, Plasmonics **2**, p. 55 (2007), dx.doi.org/10.1007/s11468-007-9027-x. 20, 59

[Bel06] S. E. J. Bell and N. M. S. Sirimuthu, *Surface-Enhanced Raman Spectroscopy (SERS) for Sub-Micromolar Detection of DNA/RNA Mononucleotides*, Journal of the American Chemical Society **128**(49), p. 15580 (2006), dx.doi.org/10.1021/ja066263w. 45, 51, 54, 57

[Bev03] M. R. Beversluis, A. Bouhelier and L. Novotny, *Continuum Generation from Single Gold Nanostructures through Near-Field Mediated Intraband Transitions*, Physical Review B **68**, p. 115433 (2003), dx.doi.org/10.1103/PhysRevB.68.115433. 16

[Böh07] M. Böhmler, *Neuartige Spitzen für die optische Nahfeldmikroskopie*, Diploma thesis, University of Tübingen, Germany (2007). 28

[Bin82] G. Binnig, H. Rohrer, C. Gerber and E. Weibel, *Surface Studies by Scanning Tunneling Microscopy*, Physical Review Letters **49**(1), p. 57 (1982), dx.doi.org/10.1103/PhysRevLett.49.57. 1, 27

[Bin86] G. Binnig, C. F. Quate and C. Gerber, *Atomic Force Microscope*, Physical Review Letters **56**(9), p. 930 (1986), dx.doi.org/10.1103/PhysRevLett.56.930. 1, 26

[Bül10a] A. K. Büll, J. R. Blundell, C. M. Dobson, M. E. Welland, E. M. Terentjev and T. P. J. Knowles, *Frequency Factors in a Landscape Model of Filamentous Protein Aggregation*, Physical Review Letters **104**(22), p. 228101 (2010), dx.doi.org/10.1103/PhysRevLett.104.228101. 59

[Bül10b] A. K. Büll, D. A. White, C. Meier, M. E. Welland, T. P. J. Knowles and C. M. Dobson, *Surface Attachment of Protein Fibrils via Covalent Modification Strategies*, The Journal of Physical Chemistry B **114**(34), p. 10925 (2010), dx.doi.org/10.1021/jp101579n. 59

[Bül11] A. Büll, *On the Kinetics of Protein Misfolding and Aggregation*, Doctorate thesis, University of Cambridge, UK (2011). 59

[Bon07] J. Boneberg, J. König-Birk, H.-J. Münzer, P. Leiderer, K. L. Shuford and G. C. Schatz, *Optical Near-Fields of Triangular Nanostructures*, Applied Physics A: Materials Science & Processing **89**(2), p. 299 (2007), dx.doi.org/10.1007/s00339-007-4138-y. 17, 35, 37, 46, 64

[Boy82] I. W. Boyd and J. I. B. Wilson, *A Study of Thin Silicon Dioxide Films Using Infrared Absorption Techniques*, Journal of Applied Physics **53**(6), p. 4166 (1982), dx.doi.org/10.1063/1.331239. 43

[Bra07] K. Braun, *Aufbau und Charakterisierung eines Nahfeldmoduls für nahfeldoptische Untersuchungen in einem Parabolspiegelmikroskop*, Diploma thesis, University of Tübingen, Germany (2007). 27

[Bur97] F. Burmeister, C. Schäfle, T. Matthes, M. Böhmisch, J. Boneberg and P. Leiderer, *Colloid Monolayers as Versatile Lithographic Masks*, Langmuir **13**(11), p. 2983 (1997), dx.doi.org/10.1021/la9621123, http://pubs.acs.org/doi/pdf/10.1021/la9621123. 35, 37

[Cam98] A. Campion and P. Kambhampati, *Surface-Enhanced Raman Scattering*, Chemical Society Reviews **27**(4), p. 241 (1998), dx.doi.org/10.1039/a827241z. 16

[Cam08] J. P. Camden, J. A. Dieringer, J. Zhao and R. P. Van Duyne, *Controlled Plasmonic Nanostructures for Surface-Enhanced Spectroscopy and Sensing*, Accounts of Chemical Research **41**(12, Sp. Iss. SI), p. 1653 (2008), dx.doi.org/10.1021/ar800041s. 17

[Cho08] I.-H. Chou, M. Benford, H. T. Beier, G. L. Cote, M. Wang, N. Jing, J. Kameoka and T. A. Good, *Nanofluidic Biosensing for Beta-Amyloid Detection Using Surface Enhanced Raman Spectroscopy*, Nano Letters **8**(6), p. 1729 (2008), dx.doi.org/10.1021/nl0808132. 20, 59, 62

[Dec09] V. Deckert, *Tip-Enhanced Raman Spectroscopy*, Journal of Raman Spectroscopy **40**(10), p. 1336 (2009), dx.doi.org/10.1002/jrs.2452. 3, 63

[DG10] T. Deckert-Gaudig, E. Kämmer and V. Deckert, *A New Approach to Sequence Proteins: TERS on Insulin Fibrils*, AIP Conference Proceedings **1267**(1), p. 1261 (2010), dx.doi.org/10.1063/1.3482414. 20, 59, 62

[Dob03] C. M. Dobson, *Protein Folding and Misfolding*, Nature **426**(6968), p. 884 (2003), dx.doi.org/10.1038/nature02261. 4, 19, 59, 60

[Dom07] K. F. Domke, D. Zhang and B. Pettinger, *Tip-Enhanced Raman Spectra of Picomole Quantities of DNA Nucleobases at Au(111)*, Journal of the American Chemical Society **129**(21), p. 6708 (2007), dx.doi.org/10.1021/ja071107q. 18, 54, 57

[Dom10] K. F. Domke and B. Pettinger, *Studying Surface Chemistry Beyond the Diffraction Limit: 10 Years of TERS*, ChemPhysChem **11**(7), p. 1365 (2010), dx.doi.org/10.1002/cphc.200900975. 1, 3, 16, 63

[Dor03] R. Dorn, S. Quabis and G. Leuchs, *Sharper Focus for a Radially Polarized Light Beam*, Physical Review Letters **91**(23), p. 233901 (2003), dx.doi.org/10.1103/PhysRevLett.91.233901. 23, 24

[Dor10] J. Dorfmüller, R. Vogelgesang, W. Khunsin, C. Rockstuhl, C. Etrich and K. Kern, *Plasmonic Nanowire Antennas: Experiment, Simulation, and Theory*, Nano Letters **10**(9), p. 3596 (2010), dx.doi.org/10.1021/nl101921y. 11

[Fis81] U. C. Fischer and H. P. Zingsheim, *Submicroscopic Pattern Replication with Visible Light*, Journal of Vacuum Science and Technology **19**(4), p. 881 (1981), dx.doi.org/10.1116/1.571227. 16, 35

[Fle74] M. Fleischmann, P. J. Hendra and A. J. McQuillan, *Raman Spectra of Pyridine Adsorbed at a Silver Electrode*, Chemical Physics Letters **26**(2), p. 163 (1974), dx.doi.org/10.1016/0009-2614(74)85388-1. 15

[Fle08] M. Fleischer, C. Stanciu, F. Stade, J. Stadler, K. Braun, A. Heeren, M. Haeffner, D. P. Kern and A. J. Meixner, *Three-Dimensional Optical*

Antennas: Nanocones in an Apertureless Scanning Near-Field Microscope, Applied Physics Letters **93**(11), p. 111114 (2008), dx.doi.org/10.1063/1.2987485. 29

[Gar10] P. Garrigan, C. P. Ratliff, J. M. Klein, P. Sterling, D. H. Brainard and V. Balasubramanian, *Design of a Trichromatic Cone Array*, PLoS Computational Biology **6**(2), p. e1000677 (2010), dx.doi.org/10.1371/journal.pcbi.1000677. 1

[Gel11] T. Geldhauser, S. Ikegaya, A. Kolloch, N. Murazawa, K. Ueno, J. Boneberg, P. Leiderer, E. Scheer and H. Misawa, *Visualization of Near-Field Enhancements of Gold Triangles by Nonlinear Photopolymerization*, Plasmonics **6**, p. 207 (2011), dx.doi.org/10.1007/s11468-010-9189-9. 17

[Gie02] B. Giese and D. McNaughton, *Surface-Enhanced Raman Spectroscopic and Density Functional Theory Study of Adenine Adsorption to Silver Surfaces*, The Journal of Physical Chemistry B **106**(1), p. 101 (2002), dx.doi.org/10.1021/jp010789f. 45, 51, 54, 57

[Gol07] B. Goldberg, *Nanophotonics and Nanoplasmonics – Control of Light at One Hundredth of the Wavelength*, Presentation (2007). 2

[Gon03] M. R. Goncalves and O. Marti, *Experimental Observation of the Scattering of Light by Planar Metallic Nanoparticles*, New Journal of Physics **5**(1), p. 160 (2003), dx.doi.org/10.1088/1367-2630/5/1/160. 17, 37

[Gro10] L. Gross, F. Mohn, N. Moll, G. Meyer, R. Ebel, W. M. Abdel-Mageed and M. Jaspars, *Organic Structure Determination Using Atomic-Resolution Scanning Probe Microscopy*, Nature Chemistry **2**(10), p. 821 (2010), dx.doi.org/10.1038/NCHEM.765. 1, 52

[Ham08] N. D. Hammer, X. Wang, B. A. McGuffie and M. R. Chapman, *Amyloids: Friend or Foe?*, Journal of Alzheimer's Disease **13**(4), p. 407 (2008). 4, 59

[Han96] H. G. Hansma and D. E. Laney, *DNA Binding to Mica Correlates with Cationic Radius: Assay by Atomic Force Microscopy*, Biophysical Journal **70**(4), p. 1933 (1996), dx.doi.org/10.1016/S0006-3495(96)79757-6. 52

[Har03] A. Hartschuh, E. J. Sánchez, X. S. Xie and L. Novotny, *High-Resolution Near-Field Raman Microscopy of Single-Walled Carbon Nanotubes*, Physical Review Letters **90**(9), p. 095503 (2003), dx.doi.org/10.1103/PhysRevLett.90.095503. 3, 13

[Har08] A. Hartschuh, *Tip-Enhanced Near-Field Optical Microscopy*, Angewandte Chemie International Edition **47**(43), p. 8178 (2008), dx.doi.org/10.1002/anie.200801605. 3, 16, 63

[Hay03] C. L. Haynes and R. P. Van Duyne, *Plasmon-Sampled Surface-Enhanced Raman Excitation Spectroscopy*, The Journal of Physical Chemistry B **107**(30), p. 7426 (2003), dx.doi.org/10.1021/jp027749b. 17

[Hay05] C. L. Haynes, A. D. McFarland and R. P. Van Duyne, *Surface-Enhanced Raman Spectroscopy*, Analytical Chemistry **77**(17), p. 338A (2005), dx.doi.org/10.1021/ac053456d. 15

[Hel94] S. W. Hell and J. Wichmann, *Breaking the Diffraction Resolution Limit by Stimulated Emission: Stimulated-Emission-Depletion Fluorescence Microscopy*, Optics Letters **19**(11), p. 780 (1994), dx.doi.org/10.1364/OL.19.000780. 7

[Hen10] L. E. Hennemann, A. J. Meixner and D. Zhang, *Surface- and Tip-Enhanced Raman Spectroscopy of DNA*, Spectroscopy **24**(1-2), p. 119 (2010), dx.doi.org/10.3233/SPE-2010-0416. 49

[Hor07] I. Horcas, R. Fernandez, J. M. Gomez-Rodriguez, J. Colchero, J. Gomez-Herrero and A. M. Baro, *WSXM: A Software for Scanning Probe Microscopy and a Tool for Nanotechnology*, Review of Scientific Intruments **78**(1), p. 013705 (2007), dx.doi.org/10.1063/1.2432410. 33, 52

[Jea77] D. L. Jeanmaire and R. P. Van Duyne, *Surface Raman Spectroelectrochemistry: Part I. Heterocyclic, Aromatic, and Aliphatic Amines Adsorbed on the Anodized Silver Electrode*, Journal of Electroanalytical Chemistry and Interfacial Electrochemistry **84**(1), p. 1 (1977), dx.doi.org/10.1016/S0022-0728(77)80224-6. 15

[Jel87] D. A. Jelski and T. F. George, *The Plasmon Dispersion Relation on a Rough Surface: A Simple Approximation*, The Journal of Physical Chemistry **91**(14), p. 3779 (1987), dx.doi.org/10.1021/j100298a013. 8

[Jen99] T. R. Jensen, M. L. Duval, K. L. Kelly, A. A. Lazarides, G. C. Schatz and R. P. Van Duyne, *Nanosphere Lithography: Effect of the External Dielectric Medium on the Surface Plasmon Resonance Spectrum of a Periodic Array of Silver Nanoparticles*, The Journal of Physical Chemistry B **103**(45), p. 9846 (1999), dx.doi.org/10.1021/jp9926802. 17

[Jen00] T. R. Jensen, M. D. Malinsky, C. L. Haynes and R. P. Van Duyne, *Nanosphere Lithography: Tunable Localized Surface Plasmon Resonance Spectra of Silver Nanoparticles*, The Journal of Physical Chemistry B **104**(45), p. 10549 (2000), dx.doi.org/10.1021/jp002435e. 17

[Jun09] J. Jung, T. Søndergaard and S. I. Bozhevolnyi, *Gap Plasmon-Polariton Nanoresonators: Scattering Enhancement and Launching of Surface Plasmon Polaritons*, Physical Review B **79**(3), p. 035401 (2009), dx.doi.org/10.1103/PhysRevB.79.035401. 13

[Kar95] K. Karrai and R. D. Grober, *Piezoelectric Tip-Sample Distance Control for Near Field Optical Microscopes*, Applied Physics Letters **66**(14), p. 1842 (1995), dx.doi.org/10.1063/1.113340. 26

[KB07] J. König-Birk, *Nahfeldphotographie mit kurzen Laserpulsen*, Doctorate thesis, University of Konstanz, Germany (2007). 35

[Ke05] W. Ke, D. Zhou, J. Wu and K. Ji, *Surface-Enhanced Raman Spectra of Calf Thymus DNA Adsorbed on Concentrated Silver Colloid*, Applied Spectroscopy **59**(4), p. 418 (2005), dx.doi.org/10.1366/0003702053641487. 45, 51, 54, 57

[Kim04] J. M. Kim, T. Hirose, S. Sugiyama, T. Ohtani and H. Muramatsu, *Visualizing a Hybridized PNA Probe on a DNA Molecule with Near-Field Optical Microscopy*, Nano Letters **4**(11), p. 2091 (2004), dx.doi.org/10.1021/nl048886i. 18

[Kim09] H. C. Kim and X. Cheng, *SERS-Active Substrate Based on Gap Surface Plasmon Polaritons*, Optics Express **17**(20), p. 17234 (2009), dx.doi.org/10.1364/OE.17.017234. 13

[Kne99] K. Kneipp, H. Kneipp, I. Itzkan, R. R. Dasari and M. S. Feld, *Ultrasensitive Chemical Analysis by Raman Spectroscopy*, Chemical Reviews **99**(10), p. 2957 (1999), dx.doi.org/10.1021/cr980133r. 14, 15

[Kol11] A. Kolloch, T. Geldhauser, K. Ueno, H. Misawa, J. Boneberg, A. Plech and P. Leiderer, *Femtosecond and Picosecond Near-Field Ablation of Gold Nanotriangles: Nanostructuring and Nanomelting*, Applied Physics A: Materials Science & Processing **104**(3), p. 793 (2011), dx.doi.org/10.1007/s00339-011-6443-8. 11, 17, 35, 46

[Kre71] E. Kretschmann, *Die Bestimmung optischer Konstanten von Metallen durch Anregung von Oberflächenplasmaschwingungen*, Zeitschrift für Physik A Hadrons and Nuclei **241**, p. 313 (1971), dx.doi.org/10.1007/BF01395428. 8

[Kre95] U. Kreibig and M. Vollmer, *Optical Properties of Metal Clusters*, Volume 25, Springer-Verlag: Berlin, Heidelberg, Germany (1995). 9

[Lei04] P. Leiderer, C. Bartels, J. König-Birk, M. Mosbacher and J. Boneberg, *Imaging Optical Near-Fields of Nanostructures*, Applied Physics Letters **85**(22), p. 5370 (2004), dx.doi.org/10.1063/1.1819990. 17, 35

[Lie01] M. A. Lieb and A. J. Meixner, *A High Numerical Aperture Parabolic Mirror as Imaging Device for Confocal Microscopy*, Optics Express **8**(7), p. 458 (2001), dx.doi.org/10.1364/OE.8.000458. 23, 24, 39

[Loe72] O. Loebich, *The Optical Properties of Gold*, Gold Bulletin **5**, p. 2 (1972), dx.doi.org/10.1007/BF03215148. 51

[Lom86] J. R. Lombardi, R. L. Birke, T. Lu and J. Xu, *Charge-Transfer Theory of Surface Enhanced Raman Spectroscopy: Herzberg-Teller Contributions*, The Journal of Chemical Physics **84**(8), p. 4174 (1986), dx.doi.org/10.1063/1.450037. 15

[Lom08] J. R. Lombardi and R. L. Birke, *A Unified Approach to Surface-Enhanced Raman Spectroscopy*, The Journal of Physical Chemistry C **112**(14), p. 5605 (2008), dx.doi.org/10.1021/jp800167v. 15, 16, 45, 54

[Ma06] Z. Ma, J. M. Gerton, L. A. Wade and S. R. Quake, *Fluorescence Near-Field Microscopy of DNA at Sub-10 nm Resolution*, Physical Review Letters **97**(26), p. 260801 (2006), dx.doi.org/10.1103/PhysRevLett.97.260801. 18

[Mal01] M. D. Malinsky, K. L. Kelly, G. C. Schatz and R. P. Van Duyne, *Nanosphere Lithography: Effect of Substrate on the Localized Surface Plasmon Resonance Spectrum of Silver Nanoparticles*, The Journal of Physical Chemistry B **105**(12), p. 2343 (2001), dx.doi.org/10.1021/jp002906x. 17

[Mei94] A. J. Meixner, M. A. Bopp and G. Tarrach, *Direct Measurement of Standing Evanescent Waves with a Photon-Scanning Tunneling Microscope*, Applied Optics **33**(34), p. 7995 (1994), dx.doi.org/10.1364/AO.33.007995. 12

[Müh05] P. Mühlschlegel, H.-J. Eisler, O. J. F. Martin, B. Hecht and D. W. Pohl, *Resonant Optical Antennas*, Science **308**(5728), p. 1607 (2005), dx.doi.org/10.1126/science.1111886. 11

[Mie08] G. Mie, *Beiträge zur Optik trüber Medien, speziell kolloidaler Metallösungen*, Annalen der Physik **330**(3), p. 377 (1908), dx.doi.org/10.1002/andp.19083300302. 10

[Nel10] J. Nelayah, M. Kociak, O. Stephan, N. Geuquet, L. Henrard, F. J. Garcia de Abajo, I. Pastoriza-Santos, L. M. Liz-Marzan and C. Colliex, *Two-Dimensional Quasistatic Stationary Short Range Surface Plasmons in Flat Nanoprisms*, Nano Letters **10**(3), p. 902 (2010), dx.doi.org/10.1021/nl903653x. 17, 41

[Neu11] L. Neumann, Y. Pang, A. Houyou, M. L. Juan, R. Gordon and N. F. van Hulst, *Extraordinary Optical Transmission Brightens Near-Field Fiber Probe*, Nano Letters **11**(2), p. 355 (2011), dx.doi.org/10.1021/nl102657m. 2, 12

[Nov97] L. Novotny, R. X. Bian and X. S. Xie, *Theory of Nanometric Optical Tweezers*, Physical Review Letters **79**(4), p. 645 (1997), dx.doi.org/10.1103/PhysRevLett.79.645. 12, 13

[Nov98] L. Novotny, E. J. Sánchez and X. S. Xie, *Near-Field Optical Imaging Using Metal Tips Illuminated By Higher-Order Hermite-Gaussian Beams*, Ultramicroscopy **71**(1-4), p. 21 (1998), dx.doi.org/10.1016/S0304-3991(97)00077-6. 12

[Nov06] L. Novotny and B. Hecht, *Principles of Nano-Optics*, Cambridge University Press: Cambridge, UK (2006). 11

[Nov07] L. Novotny, *The History of Near-Field Optics*, Volume 50 of *Progress in Optics*, p. 137 – 184, Elsevier (2007), dx.doi.org/10.1016/S0079-6638(07)50005-3. 3

[Ort07] C. Ortiz, D. Zhang, A. E. Ribbe, Y. Xie and D. Ben-Amotz, *Analysis of Insulin Amyloid Fibrils by Raman Spectroscopy*, Biophysical Chemistry **128**(2-3), p. 150 (2007), dx.doi.org/10.1016/j.bpc.2007.03.012. 20, 59, 62

[Ott86] C. Otto, T. J. J. van den Tweel, F. F. M. de Mul and J. Greve, *Surface-Enhanced Raman Spectroscopy of DNA Bases*, Journal of Raman Spectroscopy **17**(3), p. 289 (1986), dx.doi.org/10.1002/jrs.1250170311. 45, 51, 54, 57

[Pal98] E. D. Palik (Editor), *Handbook of Optical Constants of Solids III*, Academic Press: San Diego, USA (1998). 43

[Pas03] D. Pastré, O. Piétrement, S. Fusil, F. Landousy, J. Jeusset, M.-O. David, L. Hamon, E. Le Cam and A. Zozime, *Adsorption of DNA to Mica Mediated by Divalent Counterions: A Theoretical and Experimental Study*, Biophysical Journal **85**(4), p. 2507 (2003), dx.doi.org/10.1016/S0006-3495(03)74673-6. 52

[Pet04] B. Pettinger, B. Ren, G. Picardi, R. Schuster and G. Ertl, *Nanoscale Probing of Adsorbed Species by Tip-Enhanced Raman Spectroscopy*, Physical Review Letters **92**, p. 096101 (2004), dx.doi.org/10.1103/PhysRevLett.92.096101. 13

[Pet09] B. Pettinger, K. F. Domke, D. Zhang, G. Picardi and R. Schuster, *Tip-Enhanced Raman Scattering: Influence of the Tip-Surface Geometry on Optical Resonance and Enhancement*, Surface Science **603**(10-12), p. 1335 (2009), dx.doi.org/10.1016/j.susc.2008.08.033. 13

[Poh84] D. W. Pohl, W. Denk and M. Lanz, *Optical Stethoscopy: Image Recording with Resolution Lambda/20*, Applied Physics Letters **44**(7), p. 651 (1984), dx.doi.org/10.1063/1.94865. 2, 12

[Rae88] H. Raether, *Surface Plasmons on Smooth and Rough Surfaces and on Gratings*, Springer-Verlag: Berlin, Heidelberg, Germany (1988). 8

[Ram28] C. V. Raman, *A New Radiation*, Indian Journal of Physics **2**, p. 387 (1928). 1, 14

[Ran08] M. Rang, A. C. Jones, F. Zhou, Z.-Y. Li, B. J. Wiley, Y. Xia and M. B. Raschke, *Optical Near-Field Mapping of Plasmonic Nanoprisms*, Nano Letters **8**(10), p. 3357 (2008), dx.doi.org/10.1021/nl801808b. 17

[Ras06] A. Rasmussen and V. Deckert, *Surface- and Tip-Enhanced Raman Scattering of DNA Components*, Journal of Raman Spectroscopy **37**(1-3), p. 311 (2006), dx.doi.org/10.1002/jrs.1480. 18

[Ray96] Lord Rayleigh, *On The Theory of Optical Images with Special Reference to the Microscope*, Philosophical Magazine Series 5 **42**, p. 167 (1896), dx.doi.org/10.1080/14786449608620902. 8

[Sac08a] M. Sackrow, *Confocal and Near-Field Measurements with a Parabolic Mirror*, Doctorate thesis, University of Tübingen, Germany (2008). 4, 27

[Sac08b] M. Sackrow, C. Stanciu, M. A. Lieb and A. J. Meixner, *Imaging Nanometre-Sized Hot Spots on Smooth Au Films with High-Resolution Tip-Enhanced Luminescence and Raman Near-Field Optical Microscopy*, ChemPhysChem **9**(2), p. 316 (2008), dx.doi.org/10.1002/cphc.200700723. 13, 16

[Sai09] Y. Saito, P. Verma, K. Masui, Y. Inouye and S. Kawata, *Nano-Scale Analysis of Graphene Layers by Tip-Enhanced Near-Field Raman Spectroscopy*, Journal of Raman Spectroscopy **40**(10), p. 1434 (2009), dx.doi.org/10.1002/jrs.2366. 3

[Sch06] G. C. Schatz, M. A. Young and R. P. Van Duyne, *Surface-Enhanced Raman Scattering: Physics and Applications*, Chapter *Electromagnetic Mechanism of SERS*, p. 19–46, Springer-Verlag: Berlin Heidelberg (2006), dx.doi.org/10.1002/0470027320.s0601. 15, 17

[Sip00] J. D. Sipe and A. S. Cohen, *Review: History of the Amyloid Fibril*, Journal of Structural Biology **130**(2-3), p. 88 (2000), dx.doi.org/10.1006/jsbi.2000.4221. 19, 20

[Stö00] R. M. Stöckle, Y. D. Suh, V. Deckert and R. Zenobi, *Nanoscale Chemical Analysis by Tip-Enhanced Raman Spectroscopy*, Chemical Physics Letters **318**(1-3), p. 131 (2000), dx.doi.org/10.1016/S0009-2614(99)01451-7. 3

[Sta07] J. Stadler, *Optische Spektroskopiemethoden und Nahfeldmessungen an einem Konfokalmikroskop mit einem Parabolspiegel als Fokussierungselement*, Diploma thesis, University of Tübingen, Germany (2007). 23

[Sta08] J. Stadler, C. Stanciu, C. Stupperich and A. J. Meixner, *Tighter Focusing with a Parabolic Mirror*, Optics Letters **33**(7), p. 681 (2008), dx.doi.org/10.1364/OL.33.000681. 24

[Sta10] J. Stadler, T. Schmid and R. Zenobi, *Nanoscale Chemical Imaging Using Top-Illumination Tip-Enhanced Raman Spectroscopy*, Nano Letters **10**(11), p. 4514 (2010), dx.doi.org/10.1021/nl102423m. 13

[Ste08] J. Steidtner and B. Pettinger, *Tip-Enhanced Raman Spectroscopy and Microscopy on Single Dye Molecules with 15 nm Resolution*, Physical Review Letters **100**(23), p. 236101 (2008), dx.doi.org/10.1103/PhysRevLett.100.236101. 3, 16

[Sti08] P. L. Stiles, J. A. Dieringer, N. C. Shah and R. P. Van Duyne, *Surface-Enhanced Raman Spectroscopy*, Annual Review of Analytical Chemistry **1**, p. 601 (2008), dx.doi.org/10.1146/annurev.anchem.1.031207.112814. 15, 17, 44, 45

[Sun05] A. Sundaramurthy, K. B. Crozier, G. S. Kino, D. P. Fromm, P. J. Schuck and W. E. Moerner, *Field Enhancement and Gap-Dependent Resonance in a System of Two Opposing Tip-to-Tip Au Nanotriangles*, Physical Review B **72**(16), p. 165409 (2005), dx.doi.org/10.1103/PhysRevB.72.165409. 4, 13

[Syn28] E. H. Synge, *A Suggested Method for Extending the Microscopic Resolution into the Ultramicroscopic Region*, Philosophical Magazine Series 7 **6**(35), p. 356 (1928), dx.doi.org/10.1080/14786440808564615. 2, 12

[Syn32] E. H. Synge, *An Application of Piezo-Electricity to Microscopy*, Philosophical Magazine Series 7 **13**(83), p. 297 (1932), dx.doi.org/10.1080/14786443209461931. 2

[Tan09] H. Tanaka and T. Kawai, *Partial Sequencing of a Single DNA Molecule with a Scanning Tunnelling Microscope*, Nature Nanotechnology **4**(8), p. 518 (2009), dx.doi.org/10.1038/nnano.2009.155. 1

[Wag95] P. Wagner, M. Hegner, H.-J. Guentherodt and G. Semenza, *Formation and in Situ Modification of Monolayers Chemisorbed on Ultraflat Template-Stripped Gold Surface*, Langmuir **11**(10), p. 3867 (1995), dx.doi.org/10.1021/la00010a043. 59

[Wan10] X. Wang, D. Zhang, K. Braun, H.-J. Egelhaaf, C. J. Brabec and A. J. Meixner, *High-Resolution Spectroscopic Mapping of the Chemical Contrast*

from Nanometer Domains in P3HT:PCBM Organic Blend Films for Solar-Cell Applications, Advanced Functional Materials **20**(3), p. 492 (2010), dx.doi.org/10.1002/adfm.200901930. 3, 64

[Wat53] J. Watson and F. Crick, *Molecular Structure of Nucleic Acids*, Nature **171**, p. 737738 (1953), dx.doi.org/10.1038/171737a0. 4

[Wau44] D. F. Waugh, *The Linkage of Corpuscular Protein Molecules. I. A Fibrous Modification of Insulin*, Journal of the American Chemical Society **66**(4), p. 663 (1944), dx.doi.org/10.1021/ja01232a516. 20

[Web07] S. Weber, *Laserinduced Nanobubbles*, Diploma thesis, University of Konstanz, Germany (2007). 9

[Wes85] J. Wessel, *Surface-Enhanced Optical Microscopy*, Journal of the Optical Society of America B **2**(9), p. 1538 (1985), dx.doi.org/10.1364/JOSAB.2.001538. 2

[Whi09] D. A. White, A. K. Büll, C. M. Dobson, M. E. Welland and T. P. Knowles, *Biosensor-Based Label-Free Assays of Amyloid Growth*, FEBS Letters **583**(16), p. 2587 (2009), dx.doi.org/10.1016/j.febslet.2009.06.008. 59

[Zen92] F. Zenhausern, M. Adrian, B. T. Heggeler-Bordier, R. Emch, M. Jobin, M. Taborelli and P. Descouts, *Imaging of DNA by Scanning Force Microscopy*, Journal of Structural Biology **108**(1), p. 69 (1992), dx.doi.org/10.1016/1047-8477(92)90008-X. 52

[Zen95] F. Zenhausern, Y. Martin and H. K. Wickramasinghe, *Scanning Interferometric Apertureless Microscopy: Optical Imaging at 10 Angstrom Resolution*, Science **269**(5227), p. 1083 (1995), dx.doi.org/10.1126/science.269.5227.1083. 3

[Zha09] D. Zhang, X. Wang, K. Braun, H.-J. Egelhaaf, M. Fleischer, L. E. Hennemann, H. Hintz, C. Stanciu, C. J. Brabec, D. P. Kern and A. J. Meixner, *Parabolic Mirror-Assisted Tip-Enhanced Spectroscopic Imaging for Non-Transparent Materials*, Journal of Raman Spectroscopy **40**(10), p. 1371 (2009), dx.doi.org/10.1002/jrs.2411. 3, 13

[Zha10] D. Zhang, U. Heinemeyer, C. Stanciu, M. Sackrow, K. Braun, L. E. Hennemann, X. Wang, R. Scholz, F. Schreiber and A. J. Meixner, *Nanoscale Spectroscopic Imaging of Organic Semiconductor Films by Plasmon-Polariton Coupling*, Physical Review Letters **104**(5), p. 056601 (2010), dx.doi.org/10.1103/PhysRevLett.104.056601. 3, 28, 55

Acknowledgements

The doctoral study documented by this thesis was conducted from December 2007 to July 2011 under the supervision of Dr. Dai Zhang and Prof. Dr. Alfred J. Meixner at the Institute of Physical and Theoretical Chemistry at the University of Tübingen. Numerous people have helped and supported me during this time. I especially want to thank the following:

Professor Alfred Meixner for supervising this work as a doctoral advisor. His keenness on parabolic mirror optics and near-field phenomena is contagious. I also thank him for always emphasizing a good working atmosphere and arranging several great excursions for the whole working group.

Dai Zhang for the direct supervision during my doctorate. Her ideas, input and inspiration were essential to me and to this work.

My thesis committee Marc Brecht, Dieter Kern and Paul Leiderer.

The members and former members of the AK Meixner group who over many years of dedicated work designed, built and refined the SNOM setup as we use it today. Among them are Catrinel Stanciu, Marcus Sackrow and Kai Braun.

The whole VG crowd. Again Kai Braun, the technical genius of our lab, for constantly expanding and improving our setup; Anke Horneber for sharing the conviction that any experiment works better to the songs of Funny van Dannen.

All my other stupendous colleagues from the AK Meixner. Amongst them Josip Mihaljevic for the beautiful triangle calculations which you can admire on page 44.

Andreas Kolloch and Alexander Büll for their indispensable skills in sample preparation and our fruitful collaboration. Professor Paul Leiderer for his enthusiasm in nano-triangle plasmonics and our discussions on the matter.

Verena Städele for mutual encouragement. Stefan Weber – who will soon be known as 'one of the ~~AFM~~ SFM gods' – for very helpful discussions. Andreas Kolloch, Stephen Riedel, Kirstin Elgass, Ursula Neu, Ancilla Neu and Eva Kirchner who did a great job in proof-reading this thesis. Mike Hettich for answering my last-minute cries for LaTeX help. Jens Koblitz for the constant support and encouragement he gave me during these last years.

Ulrike Hennemann, Enrico Capaci and Susanne Capaci-Blaser for being such a unique and wonderful and supportive family.